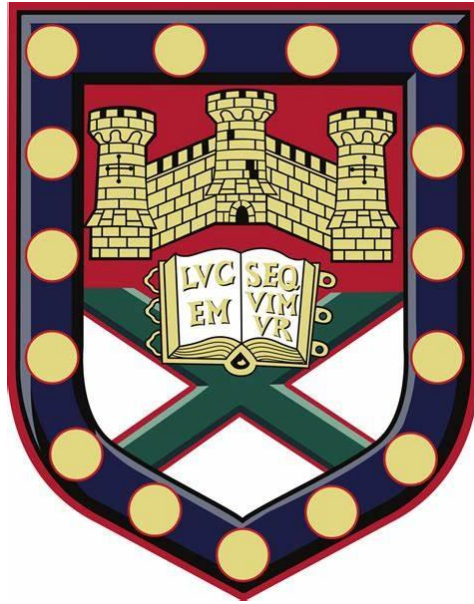


Optical observation of magnetization dynamics induced by spin-orbit torque in micro-magnetic ellipsoid.



Submitted by

Konstantinos Othon Chatzimpaloglou

to the

UNIVERSITY OF EXETER

as a dissertation for the degree of

Master of Philosophy in Physics

May 2024

This thesis is available for Library use on the understanding that it is copyright material and that no quotation from the thesis may be published without proper acknowledgement.

I certify that all material in this dissertation which is not my own work has been identified and that any material that has previously been submitted and approved for the award of a degree by this or any other University has been acknowledged.

Abstract

This Thesis presents the results of current induced magnetization dynamics driven by spin-orbit torques (SOT) in the marco-sized ellipsoid device. Devices like magnetic tunnelling junctions and spin valves are used to investigate the mechanism of spin Hall effect and Rashba effect that the understanding of the underlying mechanism can lead to higher capacity, lower power consumption and higher processing speed spin-based devices. In this Thesis, we have investigated experimentally these phenomena with different configurations employing a variety of low-frequency SOT-induced ferromagnetic resonance, or quasi-static configurations in the Time-resolved scanning Kerr microscopy (TRSKM). In addition, an analytical approach and numerical calculations were used to gain insight into the underlying mechanisms.

Devices that exploit spin currents for magnetisation reversal have recently received interest from the scientific community for their potential in non-volatile memories. Our experiments are focused on in-magnetized ellipsoids of Pt/CoFeB/MgO that present lower write currents and lower switching times. The dynamic response observed with optically detected ferromagnetic resonance configurations with TRSKM was compared with a macrospin model to understand the underlying SOT torques. Measurements with a bipolar electrical square-wave pulse to investigate the magnitude of DC SOT in micron-scale elements. The Quasi-static configuration with a magneto-optical method detects the out-of-plane magnetization directly linked with the current induced spin-orbit torque and DC Oersted field. The results presented in this Thesis from the experiments are expected to contribute to the efforts of determining the magnitude of DC induced SOT and further understanding of the underlying mechanisms in non-uniform magnetization dynamics.

One page blank

Acknowledgement

The present work in this thesis and the completion of several years of work would not have been possible without the contributions of many people. I will firstly thank my supervisor Professor Robert J. Hicken for having me under his supervision on this project and his support. His patience and insight encourage to improve from presentation to better research practices. I would like to extend my thanks to my second supervisor Dr. Paul S. Keatley, thoughtful and meaningful contributions that are valuable on this journey and beyond. Past and present members of the Magnetic Materials Group have made it a stimulating group to work in. Honourable mentions Dr. Tom H. Loughran for his supportive talks when things were going slow and his invaluable help on the technical side of the equipment. To Dr. P. Androvitsaneas for his guidance and experience has driven me on evolve faster as a scientist both in the laboratory and interpretation. To Dr. David Newman for his support as a colleague and friend and was always a calming force. From the Centre of Doctoral Training (CDT) in Metamaterials, I would like to thank Dr Ian Hooper (Pastor tutor), Dr Anja Roeding and Deb Lee for their assistance and support on various challenges and issues that I came across over the past years. I am also grateful to the efforts of David Coldridge, Nick Cole, Richard Taylor and all members of the workshop team for dealing with all manner of requests and absurd turnarounds while maintaining their cheerfulness.

Last but it means not least to my lovely family is the least I can dedicate my appreciation for how they have supported me all this time from moving away from home at 18 years old and being there every step of the way to listen and advice on my ups and downs. To my mother, for always push me to become better. My father has made appreciate me what I have. To my brother that helped over the years in numerous ways. To my friends scattered around across the world. Thank you for your unconditional support and love.

I gratefully acknowledge financial support from the Engineering and Physical Sciences Research Council (EPSRC) of the United Kingdom, via the EPSRC Centre for Doctoral Training in Metamaterials (Grant No. EP/L015331/1).

All data created during this research are available from the University of Exeter's institutional repository.

*“A bend in the road is not the end of the road
unless you fail to make the turn.”* Helen Keller

Table of Contents

Abstract	1
Acknowledgement	4
Acronyms	9
Symbol	10
1 Introduction	13
2 Background materials.....	19
2.1 Introduction	19
2.2 Magnetic moment	19
2.2.1 Spin orbit coupling	21
2.3 Ferromagnetic free energy contributions.....	22
2.3.1 Magnetostatic energy.....	22
2.3.2 Exchange energy	23
2.3.3 Zeeman energy.....	24
2.3.4 Magnetic anisotropy	25
2.4 Magneto Optical Kerr Effect (MOKE)	26
2.5 Ferromagnetic resonance	28
2.6 Anisotropic Magnetoresistance	30
2.6.1 Anomalous Hall effect	30
2.6.2 Spin Hall Effect.....	31
2.6.3 Rashba Effect	32
2.6.4 Spin-orbit torque and its applications	34
3. Experimental Techniques	36
3.1 Introduction	36
3.2 Analytical macro-spin expression	37
3.3 Magneto Transport technique	41
3.4 Time-resolved scanning Kerr measurement technique	42
3.5 Excitation of spin dynamics driven by DC and RF current to observe DC SOT	44
3.5 Observing the magnetization dynamics with bi-polar pulse	45
4. Observation of Spin-orbit torque induced ferromagnetic resonance	48
5. Quasi-static magnetization investigation for DC SOT.....	56
5.1 The Planar Hall study.....	56
5.2 Quasi-static MOKE measurement.....	59
5.3 Exploring the spatial resolution of spin dynamics.....	62

Conclusions..... 64

Acronyms

AC	Alternating Current	CMOS	Complimentary metal-oxide semiconductor
AHE	Anomalous Hall Effect	DC current	Direct Current
DMI	Dzyaloshinskii-Moriya interaction	DRAM	Dynamic Random Access Memory
FMR	Ferromagnetic Resonance	FM	Ferromagnetic layer
GMR	Giant Magneto-resistance	HAMR	Heated-assisted magnetic recording
LLG	Landau-Lifshitz-Gilbert equation	MOKE	Magneto-Optical Kerr Effect
MR	Magnetoresistance	MRAM	Magnetic Random Access Memory
MTJ	Magnetic Tunnel Junction	NM	Non-magnetic layer
RE	Rashba Effect	RF	Radio Frequency
SHE	Spin Hall Effect	SHNO	Spin Hall Nano-Oscillator
SOI	Spin orbit interaction	SOT	Spin orbit torque
STT	Spin Transfer Torque	STT-FMR	Spin Transfer Torque Ferromagnetic Resonance
TMR	Tunnel Magnetoresistance	TRSKM	Time-Resolved Scanning Kerr Microscopy

Symbol

a and b	magnetic precession amplitudes	α	Gilbert damping parameter
B	Magnetic induction field	c	speed of light
γ	gyromagnetic ratio	E	electric field
\vec{E}_z	Zeeman energy	ε	Generalized permittivity tensor
ε_0	permittivity of free space	I	Current
F_L	Lorentz force	FT	Field-like torque parameter
f	RF frequency	g	g-factor
H	Magnetic field	\hbar	Reduced Plank's constant
H_c	Coercivity field	H_d	Demagnetization field
H_{eff}	Effective magnetic field	H_{ext}	External magnetic field
H_{soi}	Spin Orbit Hamiltonian	j	Total angular momentum
j_z	The projection on the z-direction of the total angular momentum	J_c	Charge current density
J_s	Spin current density	θ	Theta angle
θ_{SH}	Spin Hall angle	$K_{1,2}$	Anisotropy constants
L	Total orbital angular momentum	l	Orbital angular momentum
\hat{l}	Orbital angular momentum number of states	l_z	orbital momentum on the z-direction
M	magnetization	\vec{m}	Magnetic moment
m_l	orbital angular momentum quantum number	m_e	Mass of the electron
μ_B	Bohr magneton	\hat{m}_s	Spin angular momentum quantum number
M_{sat}	Saturation magnetisation		
p_x	Electron momentum at x-direction	p_y	Electron momentum at y-direction

r	radius	ϕ	spatial wave function
X	Spin wavefunction	ψ	Electron wave function
q	Charge of the system	\hat{s}_{free}	Spin unit vector of the free layer
\vec{S}	Closed loop area of electrons orbits	s_{pin}	Spin unit vector of the pinned layer
ρ_{\perp}	perpendicular resistivity	ρ_{\parallel}	Parallel resistivity
$\vec{\sigma}$	electron spin polarisation	σ_{xy}^s	Transverse spin Hall conductivity
σ_{xx}^c	Longitudinal charge conductivity	φ	Phi angle
ω_0	precession frequency	Z	atomic number of the nuclei

One page blank

1 Introduction

Spintronics or spin electronics is a newly developed research field and comes from the merge of the cross-discipline of magnetism and micro-electronics. [1] New technological advancements (e.g., Heated-assisted magnetic-recording (HAMR) hard disk drive, [2,3] have contributed to pioneer developments (Artificial intelligence, Cloud data storage, computer process architecture), which require great capacities large amount of data storage, capabilities reaching as high as 12 TB [2,4] in for commercial HDD drives and low latency in processing speed. The Moore's law of microelectronics has reached previous unprecedented values for processing speeds with CMOS technology. Meanwhile, the increasing demand for higher speeds, lower power consumption and reduced size are pushing towards adopting new approaches. A promising answer solution to these current technological challenges is the non-volatile memory that fulfils the requirements for scalability, high-speed processing, robust endurance, and large storage capacity. Additionally, it has the ability to be embedded in CMOS-based chips. [2] Non-volatile memories have also been proven a promising alternative to charge semiconductor memories [5], because they can store information without the constant application of current.

The fundamental physics, that is utilised in these devices, works by exploiting the spin of electrons, rather than their charge. The spin transport is one of the most important discoveries for the data storage technology in the 20th century, that leads today's semiconductor industry. The electron is not only a charge carrier but also a carrier of spin angular momentum. In conventional charge-based electronic devices, the transport of electrons is controlled by an applied external electric field. Utilizing the spin, though, adds a degree of freedom, which was a factor not considered before. The additional degree of freedom into conventional charge-based semiconductor memories or even the usage of the spin alone, could substantially improve the performance and capability of electronic devices. This has led to the emergence and rapid progress of spintronics research and established the implementation of spintronics devices to the electronic devices of the next generation.

Compared to charge-based semiconductor devices, spintronics devices have the advantages of non-volatility, fast data processing speed, low electric power consumption and high integration densities. This potential has spurred the rapid advancement of spintronics research and established the inclusion of spintronics devices in the next generation of electronic devices.

The discoveries of giant magnetoresistance (GMR) [5–9] and tunnel magnetoresistance (TMR) [10,11] in which the electrical resistance of a material system can vary significantly depending on the orientation of magnetic moments in the ferromagnetic layers, redirected the research focus on spintronics. [11–13] Although, Magnetoresistive Random Access Memory (MRAM) still is a promising candidate to fulfil the high demand in storage capacity and processing performance, the long-term goal is a universal, non-volatile memory [14,15].

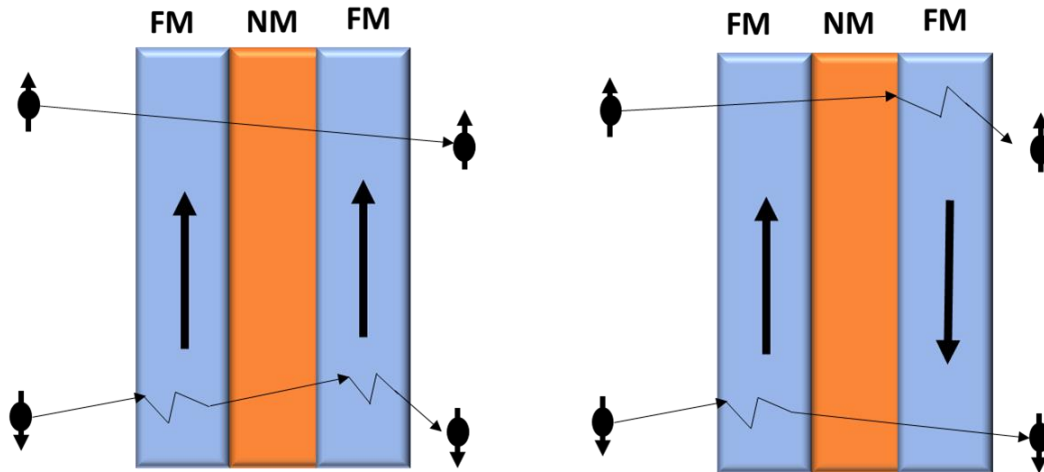


Figure 1.1: Spin valve structure present the mechanics of the Giant Magnetoresistance effect. FM. A electron from the first ferromagnetic layer (arrows show the spin orientation; long arrows show the path of the spin carriers) transfers through the nonmagnetic (NM) metal as transfer from one layer to the next.

Magnetoresistive devices are a combination of magnetic and non-magnetic layers. The key feature is that the electrical resistance of these devices depends on the magnetization orientations of the adjacent ferromagnetic layers. It has lower resistance when the magnetizations are oriented in parallel alignment and higher resistance when the magnetizations are in antiparallel alignment. [3] Consider a structure made up of three layers, with two ferromagnetic layers separated by a non-magnetic layer. The magnetic coercivity value of this structure is significantly higher than the adjacent ferromagnetic layer. As a result, when a small external magnetic field is applied, the two ferromagnetic layers can align in either parallel or anti-parallel configurations. The measured electrical resistance in such structures depends on the orientation of the adjacent layer. An example of this, it is called a spin valve structure and Fig 1.1 presents how the two FM layers function when moving electrons carry their spin angular momentum from one layer to the adjacent FM layer.

In this illustration (Fig.1.1), it is assumed that there are two spin conductance channels corresponding to the “spin up” and “spin down” states, and the resistances of the two spin channels are in parallel configuration. Due to the spin-dependent scattering, electrons with different spins will suffer different rates of scattering when flowing through a single ferromagnetic layer (FM). This will result in high resistance state when the spin orientation of the adjacent layer is antiparallel to the magnetization direction of the FM layer and low resistance state when the spin orientation is parallel to the FM layer magnetization direction for each spin channel (as indicated in Fig. 1.1).

This finding has subsequently redirected the focus on the development of devices such as the spin valve and the Magnetic tunnelling junction. The working principle in such devices is the Giant Magnetoresistance effect (GMR) and tunnelling magnetoresistance (TMR) [6,42]. Hard disk drives have incorporated these observations [6] and since the late 1990 lead the way to the innovation in storage density. [2] The further scientific investigation [5,26, 39] on spin-polarized electron

devices has shown that they have a lower power consumption and are promising candidates for providing solutions to issues of conventional electronic memories. [4,5]

This promising technology (i.e. spin-polarized electrons device) has a long history in the industry, coming from the pursuit of a prototype for universal memory. Universal memory is a single, high-performance, endurance, non-volatile memory that can serve as both execute-in-place code and data storage. [7] Ideal features for this device are the long-term data persistence and the read performance, which is required for code storage and execution. Moreover, spin-polarized electrons device has high data retention, (ten to twenty years), allowing the data to be stored without the need to move them to a storage I/O memory. [8] Recently, Everspin successfully produced a higher density 256Mb STT-MRAM has paved the way of the Gigabit era for MRAM with the announcement of the production of our 1Gb ST-DDR4 memory, with a 10-year data retention and high endurance. Commercial applications that are using Random Access Memory have a wide range of daily use devices. A list of such industrial devices is presented below, which are distinguished based on their type of RAM memory (volatile or non-volatile).

- DRAM (Dynamic Random Access Memory): A volatile memory comprised of a capacitor and transistor commonly (CMOS semiconductor technology). It requires a refresh charge to switch its bit states (charge/discharge the capacitor). While DRAM loses data quickly after being turned off, as it shows limited data remanence.
- FeRAM (Ferroelectric RAM): A non-volatile DRAM memory version with a magnetic layer replacing the dielectric layer.
- SRAM (Static RAM): A non-volatile memory that is used as common as DRAM. Although it requires power to store data, is faster than a DRAM in processing speed. This memory type stores data in another non-volatile memory in the same chip, so they are lost when the device is turned off. The saving process on a non-volatile element of the chip does not affect the processing speed.
- Flash memory: It is a type of electronic non-volatile memory, where the write or delete process are applied electrically. A MOSFET logic gate is used on the memories widely used in smartphones, USB flash drives and solid-state drives.
- Toggle MRAM:(Toggle magnetoresistive RAM) It is a magnetic tunnelling junction (MTJ) device integrated into standard CMOS chips that shows high speed in 'read' and 'write' processes with increased endurance and high reliability compared to DRAM and SRAM. The first prototype was Freescale's 4Mb MR2A16A Toggle MRAM (M. Durlam et al.,2007) by Everspins, while in March 2024 they will release the first 1GB T-MRAM (current size is 256 Mb-cite).

- STT-MRAM (Spin Transfer Magnetoresistive RAM): The newest and with the best performance on memory applications in the industry today. Samsung and Everspin have released STT-MRAM chip products with 7 MB and 25 MB capabilities. [3]

There are a few other types of RAM but the above are the most commonly used and incorporate the data storage architecture. Research work on magnetic memories aims to device a prototype of “universal memory”, that combines the best attributes of SRAM, DRAM and Flash memories. Many applications use two or three types of memories that have an impact on system performance and reliability of data transfer between different memories subsequently increasing the total cost. Furthermore, the above examples describe devices that are also implemented in the data storage industry. The most advanced chip from NVidia has been in focus as their architecture design have prosperous implementation in AI and reinforcement learning application where the CPU and GPU processing is demanding. [10] The A100 80 GB chip can reach over 2 TB if unified memory per node/element is discovered, which will also triple the performance. [11,12] The significance of “universal memory” lies in its ability to verify the achievement of full switching and, therefore, that the information has been stored. The measured voltage difference must be larger than 0.2 V so the switching of the magnetoresistance for higher to lower and vice versa are reliable.

Magnetoresistive RAM (MRAM) is currently the most promising candidate for memory with such universal characteristics. It combines non-volatility with relatively high read and write speeds and unlimited endurance. Furthermore, the MRAM storage element resides in the metal interconnect layers, well above the silicon, allowing its process to be optimized independently from the underlying semiconductor process. MRAM is therefore cost effective to integrate and is ideally suited for embedded memory applications.

Spin Transfer Torque has been a common approach to develop MRAM for fast write/read process, low power consumption and scalable memories, which can replace the embedded flash memory. STT magnetic random access memory (STT-MRAM) has been already developed by Intel and Samsung. [3] STT-MRAM devices are expected to provide advantages over the current technological solutions, and at the same time, further develop their application capabilities for higher storage capacity and faster data processing. [13] The common devices using STT torque are the magnetic tunnel junction and the spin valve. Both have a ferromagnetic layer which current passes through to a non-magnetic semi-transparent layer to reach the adjacent ferromagnetic layer. [11]

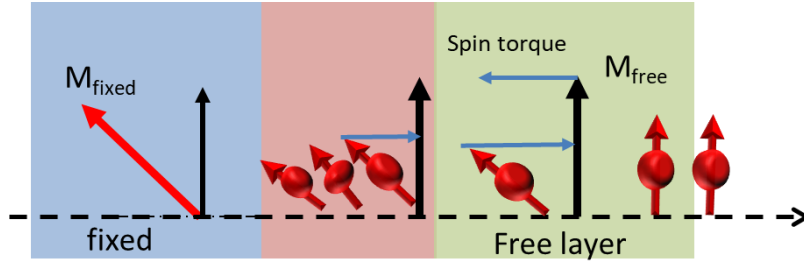


Figure 1.2: In a tri-layer structure (FM1/NM/FM2), the current pass along the device and the spin is transferred from a layer with high demagnetization value (blue - M_{fixed}) through a non-magnetic layer (light red) to the adjacent layer (light green). The spins transfer to the final layer create a spin accumulation that act on the magnetization of the adjacent layer by exerting a torque.

A magnetic tunnelling junction (MTJ) consists of two ferromagnetic metals (FM) layers separated by an ultra-thin layer of insulator to form a sandwich-like structure (FM/NM/FM), as shown in Figure 1.2. The insulating layer (IN) is so thin that the electrons can tunnel through the barrier when a bias voltage is applied between the two FM layers.

In an MTJ, usually, the orientation of magnetization in one FM layer (named pinning layer) is pinned by exchanging coupling to an antiferromagnetic layer, such as IrMn or FeMn, while the magnetization orientation in another FM layer (free layer) can be rotated by a relatively low external magnetic field. The current pass through the junction carries charge and spin angular momentum. A large current density can transfer sufficient spin carries that can exert a torque on the magnetization of the free layer, which can even fully switch its magnetization. The resistance depends on the relative orientation of magnetizations in the two FM layers, being higher in the parallel configuration and smaller resistance in the antiparallel configuration. When the NM layer is thin the electron can tunnel through the spacer layer without losing spin energy or with lower reflection from the free (FM) layer. This phenomenon is called tunnelling magnetoresistance (TMR), which is a consequence of the spin-dependent density of states. The TMR can be expressed as follows:

$$TMR = \frac{R_{AP} - R_P}{R_P} \quad (1.1)$$

where R_{AP} is the resistance of the junction with antiparallel magnetization state, and R_P is the resistance of the junction with parallel magnetization state.

More energy efficient devices and better accuracy on write and read processes are issues that await to be tackled and are currently the focus of the research efforts. The Spin-orbit torque (SOT) is a research direction that hopes to extend the lifecycle of those devices, by lowering the driving currents and reducing the writes errors. This Thesis will focus on broadening our understanding of magnetization mechanisms in these devices by conducting experiments with a Time-resolved scanning Kerr microscope. Different experimental configurations explore the local and non-local

response that induced by SOT and Oe-field. The used sample device is a micro sized magnetic ellipsoid on top of a Platinum (Hall) cross. We excited the device with the use of electrical probes and measure the Kerr signal with a balanced polarized bridge detector (stroboscopic approach). A macrospin model is used to disentangle the Oe-field contribution from the SOT contributions that we have from our measurement. The expectation is to prove that Time-Resolved Scanning Kerr Microscope (TRSKM) is a powerful tool to investigate the local spatial response in this MTJ type device.

In Chapter 2, we discussed the fundamental physical laws and principles required to understand the physics of magnetization dynamics that unfold during experiments. A simplified description of the magnetic moment is also presented. The next section introduces energy contribution terms that are interacting, so the equilibrium equation finds the energy minimization solution. A discussion on principles and equations for ferromagnetic resonance and Kerr microscopy is required to understand the experimental techniques discussed in next chapter. Furthermore, a brief description of magnetoresistance and specifically anisotropic magnetoresistance is presented. The discussion continues with an introduction of spin transfer torque (STT) and contributing effects such as the Spin Hall and the Rashba effect that are used by spin-polarized accumulated electrons to act on the magnetization.

Chapter 3 presents in detail a discussion of key experimental techniques and their applications. Furthermore, the phenomenological description of magneto-optical effects is provided to aid the understanding of TRSKM measurements. These are followed by a discussion on simple macro spin model description from a generalized form of Lifshitz-Landau-Gilbert equations, including current induced terms that are responsible for the generation of SOT torques. The optical detection Spin-orbit torque-Ferromagnetic resonance (SOT-FMR) is an experiment approach to describe the dynamic response of these devices followed by an analytical model for the interpretation of the resonance curves. The planar Hall measurements are described and used in comparison with the quasi static measurements.

Chapter 4 discusses the results of optically detected phase-resolved spin orbit ferromagnetic resonance (SOT-FMR) measurements on a microscale CoFeB ellipse at the center of a Pt Hall cross induced by RF and DC current. The field swept SOT-FMR spectra were acquired from the so-called center mode to probe the SOTs active at the center of the ellipse, thus minimizing non-uniform edge contributions. When the magnetic field was applied at 30° away from the Hard Axis (HA) of the ellipse and simultaneously applied Rf and DC current, a marked asymmetry was observed in the amplitude, resonance field and linewidth of the FMR either side of applied field polarity. Both absorptive and dispersive parts of the spectra were in good agreement with a macrospin calculation. The damping parameter α and the Slonczewski torque parameter were determined to be 0.025 and $(6.75 \pm 0.75) \times 10^7$ Oe/A/cm², respectively. The SOT-FMR linewidth is observed as almost independent of the DC current value, suggesting that the SOT has a minimal influence in the hard axis configuration.

Chapter 5 discusses the results of a quasi-static phase of the polar Kerr response. The device is excited by a square wave pulse modulated at π kHz. The torques push the magnetization out-of-plane and the MOKE response is measured as it sweeps the magnetic field. Also, the Transport Hall measurement is presented to compare them

qualitatively with the optical measurements. Moreover, it presents the calculation of a quantitative value for the SOT induced by the applied current. This is followed by the interpretation of these results, showing that DC SOT and DC Oe-field are the dominant effects and affecting the MO Kerr response. Furthermore, a direct approach is presented to measure the SOT. This is an approach to qualitative and quantitative evaluation of SOT torque by directly detecting the component of the magnetization. Concluding remarks summarizing the key findings in this Thesis.

2 Background materials

2.1 Introduction

In this chapter of the thesis, it is discussed the theoretical background and physical phenomena required to understand the field of spintronics. Furthermore, we focused on explaining the magnetic phenomena that are fundamental to understand the experimental techniques (chapter 3) and result sections (chapter 4&5) in this thesis. The concept of these phenomena, like spin-orbit interactions (SOI), requires a quantum mechanical description, to be explained properly. A description in the Magneto-Optical Kerr effect (MOKE) is delivered and followed by the mechanics of ferromagnetic resonance, which will lead to understanding the behaviour from static to dynamic magnetization response. The last section describes key phenomena, that drives the measured response that will be discussed in latter chapters. Moreover, the closing paragraph discusses spin-orbit torque (SOT) application that are presented in literature.

2.2 Magnetic moment

Historical examples of magnets like the magnetite of Thales of Miletus, or the use of an iron needle for the compass from the Chinese are few that show their feature. A magnet has two poles, commonly called north and south poles. The field of magnet has a trajectory from north to south, thus when opposite poles face each other, they attract each other while the same poles repulse. However, even though magnetic materials were discovered in ancient times, not much interest was shown in them. The most simplified example is the planetary model for hydrogen, where a single electron orbits its core nuclei. The closed loop orbit of the electrons in a circular area S . generates a current I . The magnetic moment is oriented perpendicular to the area. In the classical description, the magnetic moment is defined as:

$$\vec{m} = I \times \vec{S}. \quad (2.1)$$

The magnetic moment describes the direction of the magnetic field. The magnetic field is induced by the generated current of the moving electron.

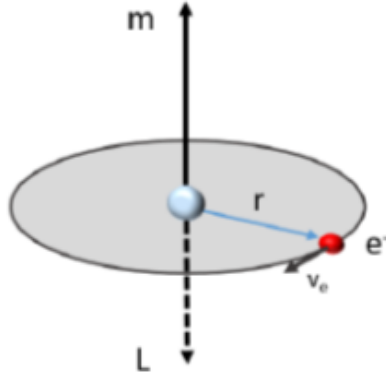


Figure 2.1: The electron orbits the positively charged nuclei. The motion generates a current that induces a magnetic moment in the perpendicular direction to the plane of motion.

The description from classic mechanics of the magnetic moment does not include the atomic spin of the electron. In the previous description, the classical description, the magnetic moment is considered as a scalar quantity; starting from equation (2.1) we replace with $I = \frac{q\omega}{2\pi}$, where q is the charge and ω is the angular frequency at a closed loop ($S = \pi r^2$). The equation in vector form is

$$\vec{m} = \frac{q\omega r^2}{2} \hat{n} \quad (2.2)$$

Since the electron orbits in a circular trajectory, its linear velocity will be equal to $v = \omega \times r$. And since the velocity and radius are perpendicular to each other, then it is $v = \omega r$. The outer product of angular velocity and radius defines the vector velocity of the electron. In this case, the angular momentum has discrete values. In the case of quantum mechanics those discrete values take the form of the equation

$$\hat{m}_l = -\frac{\hbar e}{2m_e} \hat{l} \quad (2.3)$$

where \hat{l} represents a quantum number of orbital states and \hat{m}_l is the quantum number of orbital angular momentum. Quantum mechanics has predicted the contribution of an additional electron's angular momentum which is called spin, and it is twice the size of the orbital one.

$$\hat{m}_s = -\frac{\hbar e}{m_e} \hat{s} \quad (2.4)$$

Where \hat{s} is the intrinsic spin angular momentum of the electron. As it a quantum mechanical quantity, it has not a classical description. The $\frac{\hbar e}{2m_e}$ is a constant quantity and is also called Bohr magneton $\mu_B = 9.27 \times 10^{-24} \text{ JT}^{-1}$. A final quantity is the total angular momentum is the combination of orbital and spin momentum. This is result from calculations that predict degenerates' states in atomic-scale structures. Furthermore, the spin magnetic momentum does not obey the same dependence on the orbital angular momentum, while in terms of absolute value is twice the magnitude.

$$\hat{j} = (\hat{l} + 2\hat{s}) \quad (2.5)$$

2.2.1 Spin orbit coupling

The spin-orbit interaction (SOI) is called the interaction between the magnetic spin and the effective magnetic field ($B_{eff} = -\frac{1}{c^2} v \times E$) from the orbital states shells caused by the electron's movement in the (material) crystal structure. The spin-orbit interaction (SOI) gives rise to magnetocrystalline anisotropy in the materials and supplies a mechanism for energy dissipation to the lattice. [15] The nucleus rotates round the electron's rest frame and the circulating charge creates a magnetic field that will interact with the orbiting spin. The spin couples to the orbital shell induced an electric field. The mathematical expression for the SOI Hamiltonian term acts as a perturbation and describes this interaction is shown below:

$$H_{soi} = \frac{Ze^2}{2m_e^2 c^2 r^3} L \cdot S \quad (2.6)$$

where m_e is the electron's mass, c is the speed of the light, Z is the atomic number of the nuclei and r is the radius of the electron orbital. The L is the total orbital momentum and S total spin magnetic moment. The motion is relative to reference frame (or rest frame) of the electron. This relative motion of the positive charged nucleus moves in orbital motion and generates a magnetic field that interacts with the electron spin. This is a configuration where SOI interaction's strength is weak. We are interested to explore stronger SOI interaction thus elements like Pt, Ta and Ir present strong SO coupling.

Furthermore, the 3d transition metals, such as Co, Ni, and Fe, have energy states are often degenerate, meaning that more than one electrons are at the same energy level. [16] The splitting of these energy levels is explained by exchange interaction and from the value of the g-factor is determined the amount separation of levels. When the g-factor is equal to 2 in a crystalline material, these L-states might be quenched because they do not contribute to the total magnetic moment when a magnetic field is applied [17]. A g-factor that differs from 2 indicates that the rise of orbital angular momentum as the expression for the g-factor states

$$g_{J_z} = \frac{\langle L_z \rangle + 2 \langle S_z \rangle}{\langle S_z \rangle} \quad (2.7)$$

where L_z and S_z are the orbital and spin quantum numbers associated with the quantization direction. The measured value g-factor is $g_e = 2.002319$ and any deviation shows the presence of an orbital moment. [16] These differences are the result of a weak spin-orbit interaction, which can result to rise of anisotropy. [18] In a strong internal field, the value of the g-factor could depend slightly on the direction of the applied magnetic field with respect to the crystal axes. As a result of the crystalline field, the orbital levels are split so that the orbital magnetic moment may be partly and perhaps completely quenched. Further, with partial quenching the orbital moment will have an angular variation determined by the symmetry of the crystal field. [18] The orbital momentum is then said to be quenched, since it will make no contribution to the magnetic moment when a field is applied. When a triplet orbital level is lowest, there

is further splitting by the spin-orbit coupling and/or by any internal electric field arise from the lattice. [16]

2.3 Ferromagnetic free energy contributions

From solid-state physics, we know that the total free energy will determine the ground state and excited (or dynamic magnetization) state based on the contributions of each energy term. This results in the vector of the magnetization laying at a direction where the energy reaches a relative minimum. The torque described by Brown's equation due to the effective fields are zero in gaussian units.

$$M \times H_{eff} = 0 \quad (2.8)$$

where M represents magnetisation, and H_{eff} the effective magnetic field in gaussian unit system. When the magnetisation aligns with the effective field there is no torque present, that is defined an equilibrium or static magnetic state. The energy contributions can be expressed in terms of the macroscopic magnetic parameters of the material and below is discussed the individual contributions.

2.3.1 Magnetostatic energy

The static magnetisation configuration is determined by competing contributions to the total magnetic free energy. Magnetostatic energy (also known as the stray field energy) relates to the magnetic field generated by the magnetic body itself. [19] This effect is much weaker than the exchange interaction but acts on a larger length scale, as such, atoms may interact as an array of magnetic dipoles. The energy density is given by

$$E_{ms} = -\frac{1}{2} H_d \cdot M \quad (2.9)$$

where the demagnetising field H_d is often written as the product of the demagnetization tensor \tilde{N} and the magnetization. [16] The tensor \tilde{N} is linked with the geometry of the sample. Different shapes can contribute to stronger or weaker demagnetising fields. This effect gives rise to magnetic shape anisotropy, where a preferred magnetisation is given from the shape of a sample, such as the ellipsoid investigated in this thesis. The magneto-static energy density term will be expressed, considering a uniformly magnetized thin-film sample, as

$$E_S = M_{sat}^2 (\hat{m} \cdot \hat{n}) \quad (2.10)$$

Where the \hat{m}, \hat{n} are unit vector of magnetization and unit vector normal to the sample plane respectively. The energy is minimized in this case when the magnetization lies on the plane of sample. Furthermore, the magnetostatic interaction is weak interaction

compared to the exchange interaction, but it acts on a longer distance. Magnetostatic energy contribution is an important contribution to the total free energy because competing (short-range) exchange interaction with magnetostatic interaction can lead to the formation of domains structures in ferromagnetic elements. [18]

2.3.2 Exchange energy

In the previous section, we discussed how a single electron orbiting an atom can generate a magnetic moment. However, this is not always the general case as most elements have multiple electrons in their external orbitals and not all materials have a completely full external orbital state. Macroscopically, electrons are positioned in energy states to provide energy minimization. The materials, for example 3d transition metals, have degenerate energy states, thus electrons have multiple options with the same energy. The different spin orientations (e.g. spin up or spin down) generate opposite magnetic moments. The uneven spin accumulation, formed by the spin-split energy band, leads to a non-zero net magnetization, known as spontaneous magnetization. Materials such as cobalt, iron, and nickel exhibit spontaneous magnetization.

Early theoretical models for ferromagnetic materials described a strong interaction between atomic magnetic moments that is not present in paramagnetic materials. [20] Weiss proposed that in the absence of a magnetic field, neighbouring magnetic moments would generate an internal field. Heisenberg provided a formal explanation, identifying this internal field as a quantum mechanical exchange interaction resulting from the Coulomb (long-range) interaction and the Pauli exclusion principle. [16]

The mathematical description of the two-body system is a simplified version of the exchange interaction and coupling of spins s_1 and s_2 orientations and spatial wavefunction. The total wavefunction of the system

$$\psi(r_i, s_i, r_j, s_j) = \psi(a, b) = \psi_1(b) \psi_2(a) \quad (2.11)$$

The a, b represents the position and spin orientation. The ψ_1 and ψ_2 are the wavefunction of the two electrons in the system that are of position and spin that can be exchanged for each particle.

$$\Psi(a, b) = \frac{1}{\sqrt{2}} [\psi_1(a)\psi_2(b) \pm \psi_1(b)\psi_2(a)] \quad (2.12)$$

Where the sign in Ψ is signposting when the equation is symmetric (plus sign) or antisymmetric (minus sign). So, any exchange of the electrons will result either

$$\Psi_s(a, b) = + \Psi_s(b, a) \quad (2.13)$$

$$\Psi_a(a, b) = -\Psi_a(b, a) \quad (2.14)$$

This result keeps the total wave function as an antisymmetric in agreement with the fermions status of electrons. Thus, there is always one function either the spin or spatial function is antisymmetric with respect to exchange, leading to two possible wave functions. The total wavefunction is described here is the product of the spatial with spin wavefunction. This creates a wavefunction that consists of two separate wavefunctions represent the spin state and spatial. The spin state is described by the two spins wavefunction that is given by a superposition of the spins and it is named singlet state.

$$X_s = \frac{1}{\sqrt{2}}(X_{s1}^\uparrow X_{s2}^\downarrow - X_{s1}^\downarrow X_{s2}^\uparrow) . \quad (2.15)$$

The arrows in superscript represent the spin state up or down and the subscript the relative spins. In the triplet state there are three spin states, owing to the three eigenvalues of the z-component of the spin quantum number ($S_z = -1, 0, \text{ or } +1$), which can be written as

$$X_T = \begin{cases} X_{s1}^\uparrow X_{s2}^\uparrow \\ \frac{1}{\sqrt{2}}(X_{s1}^\uparrow X_{s2}^\downarrow + X_{s1}^\downarrow X_{s2}^\uparrow) \\ X_{s1}^\downarrow X_{s2}^\downarrow \end{cases} \quad (2.16)$$

The triplet state is favourably energetically than singlet. In fact, when the spatial wavefunction is antisymmetric, with respect to the exchange of particle coordinates, the Coulomb energy is smaller than for the symmetric spatial wavefunction. The mechanism of exchange interaction is found at the very core of the magnetic order while it is creating a lot of confusing in solid. In the Weiss-Heisenberg model the meaning of exchange has derived from calculations on simpler molecules (i.e. H_2, He_2) while the Stoner band model has used taken the path of density functional calculations for a single spin over a sea of electrons. The energy difference between to models comes from the rise of intra-atomic Coulomb interactions.

2.3.3 Zeeman energy

There is an energy term associated with the interaction between the atomic permanent moments and an applied field called the Zeeman energy. The moments will tend to align with the field in order to reduce this energy. The term that expresses this interaction is

$$E_z = -M \cdot H \quad (2.17)$$

In a sufficiently strong field, all magnetic moments in the ferromagnetic material will align with the external field and the magnetisation will reach a maximum. In this case, the Zeeman energy term is minimised.

2.3.4 Magnetic anisotropy

The spontaneous magnetization is an inherited feature of ferromagnetic materials. It originates from spin-orbit interaction between the atomic moments in the material structures. The anisotropy energy is caused by the long-range dipole-dipole interaction and spin-orbit interaction. Due to its nature, magnetic anisotropy is distinguished into three categories the shape, the crystalline and surface anisotropy. The shape and surface anisotropy originates from the interaction of neighbouring magnetic moments (dipole-dipole interaction), while the crystalline anisotropy is due to the local spin-orbit interaction. The interacting atomic magnetic moments of the materials can give rise to magnetization energy, which ends up favours an orientation of the macroscopic magnetization aligned in one direction concerning the crystalline axis.

The crystalline structure or the shape anisotropy can provide a preference axis known as the Easy Axis (EA). [17] The orientations of the easy and hard axes can be determined by geometrical parameters such as the shape of the material or the interaction of the magnetization with the crystalline structure field. [19] The origin of this effect is complex and involves the interplay of the exchange interaction, spin-orbit interaction, and other effects. [20] Magnetization is an axial vector, while anisotropy is not a vector quantity. In simple terms, the geometry of the sample can establish a preferred orientation for the magnetization vector alignment (e.g. the long axis of the ellipsoid), but not all components of the magnetization will align fully in this direction. The energy density term of magnetic anisotropy is a power series of the trigonometric function of the angles between the magnetization and the principal axis of the sample crystal structure [22]

$$E_{ani} = K_1(m_1^2 m_2^2 + m_1^2 m_3^2 + m_2^2 m_3^2) + K_2(m_1^2 m_2^2 + m_1^2 m_3^2 + m_2^2 m_3^2) \quad (2.18)$$

where K_1 and K_2 are the first and second order anisotropy terms, respectively. The component m_i ($i=x,y,z$) is the magnetisation along any axis of the cubic structure. The anisotropy energy is zero if the field is aligned along any of the axes. We consider the ideal case when magnetization is fully aligned to the external applied field. The above relation is considered for iron (Fe) cubic structure [100]. For hexagonal cobalt, any orientation over the perpendicular axis (hard axis) and the magnetization is almost isotropic for given an angle θ defined by the magnetization direction and the symmetry axis, hence any direction on the plane perpendicular to the c-axis is a hard direction. The energy density term is modified (considering higher order negligible)

$$E_{ani} = K_1 \sin^2(\theta) + K_2 \sin^4(\theta) \quad (2.19)$$

where E_{ani} is the energy term per unit volume for uniaxial crystals. It is common to see the anisotropy energy term as trigonometric functions of angles created by the magnetization vector with the principle's crystal axis. [16] A common misconception is that uniform magnetization sample (e.g. a thin-film of single-crystal Cobalt) comes from a single magnetic domain that covers the entire specimen. [16] However, the reality is that uniform magnetization is not always energetically favoured, for example, in multilayered FM structure might not present a uniform magnetization. These static magnetic properties provide a basic description of any magnetic system, and knowledge of them is clearly needed before the dynamic properties and finite temperature behaviour can be described in ultrathin films, as discussed in later chapters.

A very common approximation considers the anisotropy as an effective field. The two atomic scale sources of magnetic anisotropy are the magnetic dipolar interaction and the spin-orbit interaction. Due to the long-range feature, the dipolar interaction results in a shape-dependent contribution to the anisotropy, which is of particular importance in thin films and is largely responsible for the in-plane magnetization usually observed. In the absence of spin-orbit interaction (quenched orbital states), the total energy of the electron-spin system is considered independent of the direction of the magnetization. In the case of strong spin-orbit interaction, a small orbital energy is an additional energy that it contributes to the relative orientation of the magnetization in the material structure axes. In simpler terms, this is considered as the magnetocrystalline anisotropy contribution. In general, the dipole-dipole interaction and spin-orbit interaction cause the equilibrium states of magnetization to shift. For the case of zero applied magnetic field, this results to the magnetization vector not to be fully aligned in a specific direction parallel to the axis. [22] A magnetic thin film can behave as a single magnetic polarized domain in absence of magnetic field is applied. If the magnetization changes occur by coherent rotations only, the hysteresis curve can be calculated by using the same methods employed for single domain particles. Therefore, in the case of the ellipsoid we consider that there is a small misalignment between applied field and magnetization, which is observed in the measurements.

2.4 Magneto Optical Kerr Effect (MOKE)

The magneto-optical Kerr effect (MOKE) may be applied to any metallic or otherwise light-absorbing magnetic material with a sufficiently smooth surface, whereas the Faraday effect is restricted to transparent media. Furthermore, I will describe the mechanism of MOKE. Let us first assume the magnetization to be oriented perpendicular to the surface. Then, a linearly polarized light beam will induce electrons to oscillate parallel to its plane of polarization—the plane of the electric field \vec{E} of the light oscillates. The reflected light is polarized in the same plane as the incident light. At the same time, the Lorentz force induces a small component of vibrational motion perpendicular to the primary motion and to the direction of magnetization. This secondary motion generates secondary amplitudes, because of Huygens' principle.

More recently, MOKE has been used to investigate ferromagnetic materials down to the nanoscale. [19,23] This technique is utilized to selectively detect a single component of the magnetization using polarized light. A linearly polarized light is

reflected from the surface of the ferromagnet under a time-varying magnetic field. The changes in the polarization on the reflection are directly proportional to the changes of the magnetization, as we sweep the magnetic field. Similarly, the (Magneto-Optical) Faraday effect, where the plane of polarization on transmission is rotated. The light later goes through a prism, named Analyzer, where a polarizing detector can sense the change of polarization as a relative voltage difference. Observing these signals, it can be understood how the magnetization behaves under the influence of external excitation (field or current).

Consider now, the magnetization to be oriented perpendicular to the surface of the material. The superposition reflection and transmission lead to magnetization-dependent polarization rotations. This effect is strongest at perpendicular incidence ($\theta = 0^\circ$). As it is demonstrated in the figure 2.2 caption, it consists of a rotation of the plane of polarization which for $\theta = 0^\circ$ is by symmetry the same for all polarization directions of the incident beam. In the other case, (fig. 2.2-right side) The light beam is at an angle relative to the surface. It yields a magneto-optical rotation both for parallel (with respect to the plane of incidence) and perpendicular polarization of the in-coming light, as it is shown by inspecting the angular relations between incident light amplitude, Lorentz motion, and reflected or transmitted light direction. For both cases the rotation direction of polarization is opposite in the two cases, clockwise and counterclockwise respectively.

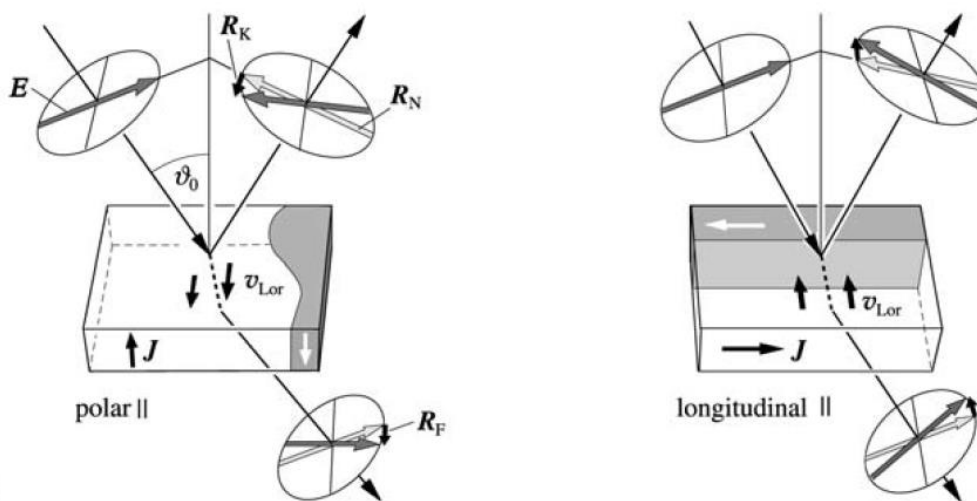


Figure 2.2: On the left is the polar and the longitudinal (on the right) magneto-optical Kerr and Faraday effects. R_N is the regular reflected electric field amplitude. A linear polarized incident light face the ferromagnet's surface on an angle ϑ_0 is then reflected (R_K) and/or transmitted (R_F) with respected optical amplitudes that are a result generated by the Lorentz motion $v_{Lor} = -m \times E$. On the left case the magnetization is within the plane of incident but perpendicular to the surface (polar Kerr configuration) and they are largely independent of the direction of polarization. On the contrast on the longitudinal configuration, the magnetization is parallel to the plane of incident and to the surface normal plane. shown here also for the parallel polarization case, increase proportional to $\sin \vartheta_0$. [19] The phase/rotation is opposite in the both cases.

There are three basic configurations in the magneto-optical Kerr effect (MOKE). The first configuration, known as the polar MOKE, detects the out-of-plane component of magnetization. The other two configurations are parallel to sample's plane. In the longitudinal effect, the magnetization lies in the plane of incidence and is parallel to the surface. The light beam must be at an angle relative to the surface. This configuration results in a magneto-optical rotation for both parallel and perpendicular

polarizations of the incoming light. The polarization of incident light is defined as the plane between the plane of oscillation of the electric field and the propagation plane. Polarization states on the reflection or transmission will be either parallel or tranverse to the incident. The third configuration, known as the transverse configuration, is weaker and does not result in rotation of the plane of polarization. Instead, it causes fluctuations in the amplitude on the reflection. In summary, on the magneto-optical technique, a beam of polarized light is either transmitted through a ferromagnetic specimen or reflected from its surface. If there is a component of magnetization along the direction of light propagation, the plane of polarization will be rotated. This rotation is known as the Magneto-Optical Faraday effect for transmitted light and the MO Kerr effect for reflected light.

2.5 Ferromagnetic resonance

Ferromagnetic resonance (FMR) is the collective motion of the magnetization (at a specific frequency or field) in a ferromagnetic material under the influence of a strong static or time-varying magnetic field. Griffiths had first observed experimentally [24] while the theoretical description was delivered by C. Kittel. [25] The equation of motion, attributed to Landau and Lifshitz [26], that describes the precession (of magnetization) along the direction of the applied magnetic field (in CGS).

$$\frac{dM}{dt} = -|\gamma|M \times H \quad (2.20)$$

Here, M is the magnetization vector, t represents time, γ the gyromagnetic ratio, and H the total magnetic field. The minus sign indicates the direction depend on the electron and the gyromagnetic ratio. The equation (2.19) is the time-dependent precessional motion of the magnetization dynamics. The solution of the zero torque, as it described mathematically in (2.7), result in a steady state precession of the magnetization vector around the magnetic field when all field components other than the external applied magnetic field are omitted. Due to the strong exchange interactions in a ferromagnet resonance phenomena tend to be coherent among atomic moments. Hence, in a field that is sufficiently strong, the precession can be viewed as a uniform response macroscopically. Additionally, the precession frequency is expressed by the Larmor frequency $\omega_L = \frac{\gamma}{2\pi} H_{ext}$.

The dynamics at the atomic level involve interactions between spins, electrons, and phonons, with energy transferred during these interactions, causing relaxation. The relaxation emerges as a damping torque which brings the precessional motion towards the applied magnetic field H_{ext} , seeking to align the magnetic moment with H_{ext} . In 1955, T. L. Gilbert reformulated the equation expressing the sum of all relaxational processes through a single damping constant as the intrinsic property of the magnetic

material—the so-called Gilbert damping α . [27] Since then, the Landau–Lifshitz–Gilbert (LLG) equation has been used to describe the dynamics

$$\frac{\partial \hat{s}}{\partial t} = \gamma(\hat{s} \times H_{eff}) + \alpha(\hat{s} \times \frac{\partial \hat{s}}{\partial t}) \quad (2.21)$$

The \hat{s} unit vector parallel to the magnetization of the system. The effective magnetic field is noted as H_{eff} , accounts for the external magnetic field, including demagnetization, the Zeeman effect, the anisotropic field, and the exchange field; the second term indicates that such a precession would eventually be damped out with the moment fully aligned with the field; γ and α are the gyromagnetic ratios and the Gilbert damping factor, respectively. The first term of the equation (2.21) describes the torque on the magnetic moment of the system causing the latter to precess at the direction of effective field. The second term is the force on the magnetic moment at the centre of elliptical precessional and dictates elliptical motion. In the case of current-driven precession in a trilayer structure (FM/NM/FM) the dynamics now affected by the presence of current-induced terms. This is the current-induced Oersted field and the Spin Transfer Torque (STT) terms that are divided into damping-like and field-like terms.

The LLG equation requires now to be reformulated, to maintain consistency with additional current induced terms representing the STT effect [28,29] The modified LLG equation, known as the LLG-Slonczewski (LLGS) equation, becomes

$$\frac{d\hat{s}}{dt} = \gamma(\hat{s} \times \mathbf{H}_{eff}) + \alpha\hat{s} \times \frac{d\hat{s}}{dt} + \gamma STI\hat{s} \times (\hat{s} \times \hat{\sigma}) + \gamma FTI(\hat{s} \times \hat{\sigma}) \quad (2.22)$$

where \hat{s} and $\hat{\sigma}$ are unit vectors parallel to the magnetization and spin polarization respectively, ST and FT are the amplitudes of the Slonczewski and field-like torque terms, the gyromagnetic ratio $\gamma = g\mu_B\hbar$, where g is the spectroscopic splitting factor, μ_B is the Bohr magneton (defined to be a negative number here due to the negative sign of the electron charge), and \hbar is Planck's constant divided by 2π . The two additional terms explicitly describe the role played by the current in either enhancing or cancelling the damping term, determined by the critical current density J_c . The scalar coefficients in these terms, ST and FT , represent the two origins of transferred torques: the Slonczewski (anti-damping) torque, and the field-like torques (FLT), respectively. Further details on the STT theory can be found in [30,31] The form of the equation is to solve the problem with one ferromagnetic layer, the spin polarization is the representation of the pinned layer.

The equation (2.21) describes a torque on the magnetisation that causes the magnetisation to precess around the direction of the effective field. As mentioned earlier, the common analogy used to describe this motion is the spinning top where the angular momentum of the top spinning on its own axis and precession about the vertical axis is described by the cross product of the angular momenta. Additional terms include the damping of the precession as the magnetisation returns to its equilibrium orientation.

This term represents a force directed toward the centre of the precession orbit and causes the magnetisation to follow a helical path. This phenomenological equation does not allow for variations of the damping that may arise with, for example, anisotropy of the material. In the case of uniform magnetisation precession, the dependence of the frequency on the field and the magnetisation is given by the Kittel equation (in Gaussian units)

$$\omega_0 = \gamma \sqrt{H(H + 4\pi M)} \quad (2.23)$$

Here, the equation is simplified as demagnetization factors are diminished and is the result for an in-magnetized samples and ignoring anisotropies within the plane. The macro-spin model was built on this theory and run numerical simulations helped us understand the optically probed phased-resolved spectrum under ferromagnetic resonance induced by SOT effect and Oe-field.

2.6 Anisotropic Magnetoresistance

Magnetoresistance (MR) is a property of materials whose electrical resistance changes when an external magnetic field is applied. Ferromagnetic materials are the best examples of this phenomenon. Anisotropic magnetoresistance (AMR) emerges from spin-orbit interactions. AMR refers to the variation of the resistance as a function of magnetization orientation relative to the current direction. It was observed that the resistance has angle dependence between

$$\rho = \rho_{\perp} + (\rho_{\parallel} - \rho_{\perp}) \cos^2 \theta \quad (2.24)$$

where ρ_{\parallel} is the resistivity observed when the magnetisation is parallel to the direction of current (where $\theta = 0$), and ρ_{\perp} is the resistivity at $\theta = 90$. It is typical for measurements to report the DC resistance V/I and the differential resistance dV/dI . The above relation explains that the max resistivity is presented when the magnetization and current direction are parallel, while minimum when they perpendicular to each other.

2.6.1 Anomalous Hall effect

In 1879, Edwin Hall discovered that materials under a magnetic field will have a transverse voltage when a current flows through the sample and perpendicular to the magnetic field. The Lorentz force acts on the charged electrons. The force acts in opposite directions depending on the carriers (i.e. electrons) of different signs. This is called the Ordinary Hall effect (OHE) for conductors/semiconductors. A similar effect was observed in ferromagnets, whereby the transverse current is dependent on the magnetisation of the material in which the current flows. This has since become known

as the Anomalous Hall Effect (AHE) and is seen to be larger than the ordinary Hall effect (sometimes orders of magnitude). The underlying mechanism for this effect is generally accepted as spin-orbit coupling, leading to a spin-dependent scattering. However, much debate remains as to the intrinsic and extrinsic contributions.

2.6.2 Spin Hall Effect

Further investigation on magnetic materials discovered that moving spin carriers can generate a transverse spin current in materials with strong spin-orbit coupling. The spin carriers will be separated depending on the orientation of their spins, this is analogous to the way the Hall effect separates charge carriers. This phenomenon has come to be known as the Spin Hall Effect (SHE) and was successfully measured in 2004 in a p-n junction device using Scanning Kerr Microscopy. [32–34] However, its extrinsic and intrinsic contributions are still under debate. The SHE strength in a material is characterized by a dimensionless parameter, the spin Hall angle

$$\theta_{SH} = \frac{J_s}{J_c} = \frac{\sigma_{xy}^s e}{\sigma_{xx}^c \hbar}. \quad (2.25)$$

Both the spin current J_s and charge current J_c are intrinsic to the material and they are connected to the conductivity tensor. [35] The symbol σ_{xy}^s represents the transverse Spin Hall conductivity (which represents the transverse spin current generated in response to an electric field) and σ_{xx}^c the longitudinal charge conductivity. Both of these properties are intrinsic to the material. The Spin Hall angle value, typically, is given in percentage value, where a positive angle indicates the spin accumulation follows the right-hand rule. This involves the vector of spin orientation (magnetic field), Lorentz force and interfacial electrons motion (velocity). For example, heavy metals, like Platinum (Pt), have a Spin Hall (SH) angle, despite a range of reported values, around $\theta_{SH} = (0.122 \pm 0.027)$. [36] This, together with the high conductivity and ease of synthesis, Platinum (Pt) or other heavy metal, is frequently used for exploiting the SHE in SOT-devices. The SHE is purely a quantum mechanical phenomenon as it arises from the spin-orbit interaction. In brief, three underlying mechanisms have been determined, that can contribute to both the SHE and the Anomalous Hall effect (AHE). These mechanisms are described and are illustrated in figure below:

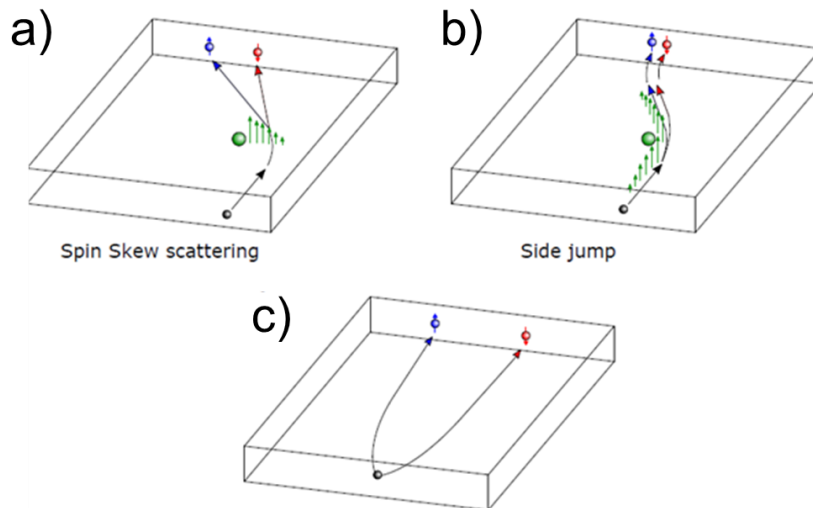


Figure 2.3: Illustration representing the mechanisms that contribute to both the Spin Hall and Anomalous Hall effects. a) Spin Skew Scattering, the spin orbit coupling gives rise to an effective field gradient, represented by the green arrows. b) Side-jump occurs due to spin-dependant acceleration and deceleration (represented by green arrows) during scattering from spin-orbit coupled impurities. c) Intrinsic Spin Hall Effects, which occur between scattering events. Copyrights: [15]

- **Spin Skew Scattering** - Spin-orbit coupling causes an effective magnetic field gradient, particles of opposite spins experience and opposite forces, hence possess different momentum. This gives rise to spin Hall effects in isotropic media.
- **Side Jump Scattering** - During scattering particles will experience both acceleration and deceleration, depending on the orientation of their spin. Particles that undergo scattering from spin-orbit coupled impurities acquire a transverse displacement.
- **Intrinsic Effects** - This refers to mechanisms that result in spin-dependent particle velocities. Especially, these mechanisms originate from the effect that spin-orbit coupling has on the electronic band structure.

The first two, the Spin Skew and the Side Jump Scattering are referred to as extrinsic effects that happen during particle scattering, while intrinsic effects act on particles between scattering events. It should be noted that if the band structure is not “spin split”, and that there is no net spin polarisation on parts of the band. This means individual spins with both polarities can be present, but only the majority dictate the magnetization amplitude and direction.

2.6.3 Rashba Effect

In semiconductor compounds with lack of inversion symmetry (e.g. GaAs or InSb), the SO coupling is reduced to a linear equation that describes a field-like term.

$$\widehat{H}_D = \frac{\beta}{\hbar} (p_x \sigma_y - p_y \sigma_x) \quad (2.26)$$

The momentum p_x, p_y describes the moving electrons in the system, and $\sigma_y \sigma_x$ is the conductivity on the x, y direction. The parameter β is a constant of the effective field. Dresselhaus et.al. proposes an explanation as an effective field (H_D) in the presence of strain along (001) direction. [16]. In thin films with broken inversion symmetry, it was first proposed by Bychkov and Rashba that an interfacial electric field $E = E \hat{z}$ will result in an effective magnetic field with the form

$$\widehat{H}_R = \frac{\alpha_R}{\hbar} (\hat{z} \times \hat{E}) \hat{\sigma} \quad (2.27)$$

where α_R is the Rashba parameter. In a structure with a lack of inversion symmetry moving electrons will experience an electric field that acts as a relativistic magnetic field H_R in their motion frame. This result was predicted from SO coupling, where the effective field can act on the atomic magnetic moment. [21] There are the interfacial and the bulk effective fields. The interfacial is also called Rashba-Bychkov effective field and the bulk is called Rashba-Eddelstein effective field.

The effective field H_R is a perturbation like the SO field. Beginning from the Lorentz force acts in a direction perpendicular to the motion of an electron with momentum p , that moves under a magnetic field B ,

$$F_L = \frac{-e}{m} \vec{p} \times \vec{B} \quad (2.28)$$

The system's Zeeman energy that arises from the magnetic field B

$$\vec{E}_z = \mu_B (\vec{\sigma} \cdot \vec{B}) \quad (2.29)$$

with $\vec{\sigma}$ represents the electron spin polarization. In contrast, a moving electron in an electric field E , can be expected in the $(p \times E)$ direction that is the direction of the effective field. The field is an effective field B_{eff}

$$B_{eff} \sim -\frac{1}{mc^2} p \times E \quad (2.30)$$

This is the field that is sensed by the electron in its reference frame. By substitution of equations (2.29) in (2.28), the Zeeman energy induced by SO coupling can be formulated as a Hamiltonian term

$$H_{so} \sim \frac{\mu_B}{mc^2} \sigma \cdot (E \times p) \quad (2.31)$$

The effective electric field of the accumulated interfacial electrons with σ spin polarization and p momentum is generated at the interface of two layers with broken inversion symmetry. In thin films, a significant portion of the moving electrons

experiences the induced electric field, that translates to a spin polarized current. The Rashba effect has been demonstrated from direct measurement to be significantly higher from the current-induced Oersted field [20] and demonstrated that can exert a (field-like) torque on the magnetization. [14,37–39] A detailed review of the Rashba effect and the association with current induced phenomena like spin-orbit torques can be found in Manchon et.al. [40] The SOT torque mechanism is still under investigation, while the major contributors to the response are defined as the SHE, driving the damping-like torque (also called a "Slonczewski torque) and the Rashba, which is linked to the transverse field-like torque.

2.6.4 Spin-orbit torque and its applications

The giant magnetoresistance effect in spin-valves was discovered in 1988 independently by P. Grünberg [41] and Albert Fert [42], to whom the 2007 Noble Prize in Physics was jointly awarded. A spin-valve is a multilayered structure, two ferromagnetic metals are separated by a conducting spacer layer. The saturation fields of the two layers are different, so an external field can switch one layer in isolation of the other, giving parallel or antiparallel magnetisation. The parallel magnetisation configuration gives lower electrical resistance than the antiparallel configuration, which can be explained by considering separate conduction channels for spin-up and spin down electrons. Conventionally, spin torques acting on the magnetization have been associated with the transfer of spin angular momentum between two layers, a 'polarizer' and a 'free' ferromagnetic layer, separated by a non-magnetic spacer, mediated by a spin-polarized current flowing perpendicular to the two layers. [43,44]

Spin transfer torque has been the preferred approach for magnetic tunnel junctions as a field-free device that can be integrated into CMOS chips. Spin-orbit torque promises to overcome the challenges of the STT-MTJ devices with scalability, fatigue of the non-magnetic layer and thermal effects. The device structure is designed such that there is a ferromagnetic layer with a fixed magnetization and a free layer that can be easily switched to be aligned parallel or anti-parallel to the orientation of the fixed layer. As a result, a spin-polarized current transfers angular momentum to the free layer, and the accumulated spin will exert a torque on the magnetization. This it is predicted that if we apply large current density, we can fully switch the magnetization. [44]

In the case of Spin-Transfer Torque (STT), the switching of magnetization occurs by passing an electrical current vertically through the stack. As electrons pass through the layers, they convert into a spin-polarized current parallel to the magnetization of the fixed layer. This spin current injected additional spin momentum into the free magnetic layer with a process referred to as spin filtering. When spacer layers are thinner than the spin diffusion length, this is possible without loss of spin. The build-up of spin in the free layer directs the magnetization towards a new equilibrium position, causing a re-orientation of the magnetization vector.

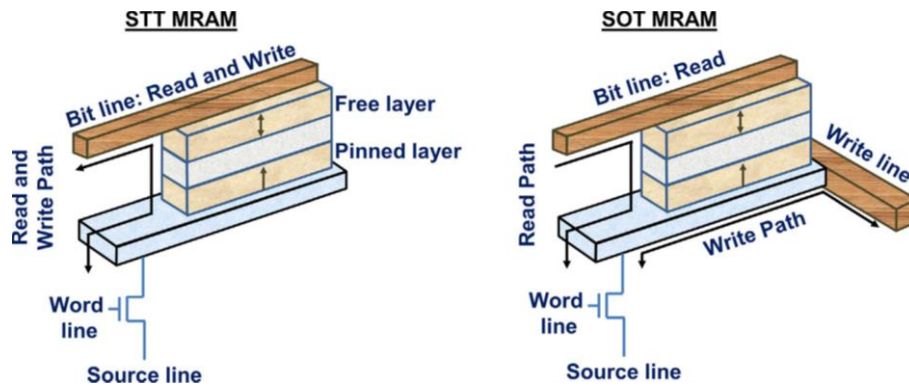


Figure 2.4: The schematics of STT- MRAM and SOT-MRAM device. A proposed prototype that enables the in-plane “write” current to pass through the less resistive metals, rather than the current passing through the resistive magnetic tunnelling junction. The smaller “read”-current is along through MTJ. (Image is from [2])

Fabrication of devices for SOT-MRAM presents advantages in their commercial applications. SOT devices promise larger overdrive currents, while high currents pass through the less resistant heavy metal (i.e. Pt, Ta, W). This is achievable by altering the path of the ‘write’ current through the heavy metal and not passing through the higher resistive MTJ. Figure 2.4 shows this difference between the “write” and smaller amplitude “read” current in STT-MRAM and SOT-MRAM. Furthermore, the SOT devices allow for direct optical access to the magnetic layer, a feature which was difficult in spin valve structures due to the placement of electrical contacts. Additionally, since the material no longer needs to be conductive, materials can be selected purely for their magnetic properties.

The origins of magneto-resistive RAM and the mechanism of SOT torques in magnetic structures were discussed. Today in literature, there are demonstrations of SOT-MRAM devices. [45] The two major types of devices are the spin valve and magnetic tunnelling junction. These multilayered structures present change to resistance to an electrical current that is dependent on the relative magnetisation between the pinned ferromagnetic layer and the free ferromagnetic layer. The principal difference between the two devices is that the spin-valve uses a conducting metallic spacer layer while an MTJ uses an insulating barrier, usually a metallic oxide. The magnetoresistance effects for the two devices are termed the GMR [41,42] and tunnelling magnetoresistance (TMR) [43], and both will be described below.

Ferromagnetic materials have been used as data storage media for several decades, and the technology continues to advance at an impressive rate. Between 1954 and 2000 hard disk data storage density increased by a factor of 10 million as bit sizes were reduced. [45] The speed of reading and writing data is also a strong driving factor in the industry. New scientific discoveries lead to innovation and exploit effects to improve efficiency and increase capacity. One of those properties was the spin-dependent conductivity of ferromagnetic metals that promise entirely new spin-based electronics with, for example, non-volatile random access magnetic memory. Major advances in the application of magnetism in both areas are the spin-valve and magnetic tunnel junction. Implementing STT and SOT approaches in MRAM prototypes has shown current control of magnetization in devices with features like

write current speed up to 0.35 nsec., retention rates over ten years and a high TMR ratio of 176%. [44,47]

The spin-valve has a conducting spacer layer and two ferromagnetic layers. The difference in resistance is termed giant magnetoresistance, with a lower resistance for the parallel magnetisation configuration and a higher for the anti-parallel. A magnetic tunnel junction (MTJ) is essentially a spin-valve with a thin (1-2 nm) insulating spacer layer, however, the process of magnetoresistance is rather different. Instead of conduction electrons experiencing a different electrical resistance in each ferromagnetic layer, in an MTJ the magnetoresistance is determined by the probability of electrons tunnelling across the barrier layer. Tunnelling magneto-resistance (TMR) is typically larger than magneto-resistance achievable in spin valves.

MTJs are commonly used as read heads in most hard disk drives currently available on the market. They can also serve as data storage bits in magnetic random access memory (MRAM), with the first commercial MRAM chips already being sold. MTJs can be utilized as a source and detector of spin-polarized currents, which have extensive applications in future electronic devices based on the spin of electrons rather than their charge.

In the future, it is expected that MTJs will offer higher densities compared to their volatile counterpart, SRAM, making them more suitable for data centers and battery-powered applications. [48] With a processing speed of up to 10 ns, their overall computing performance can be further enhanced when integrated with computing in memory circuit design. This technology holds great potential for applications in high-performance computing (HPC), artificial intelligence (AI), automotive chips, and more [4,47,48]

In conclusion, we have discussed the fundamental principles driving the spin-orbit mechanism, with the key building blocks for spintronics being spin valves or magnetic tunnelling junctions. The growing interest in SOT-MRAM stems from the high processing speed, robust endurance, and low power consumption required for data centers and IoT edge computing. Memory and logic spintronic devices rely on generating spin torques to control the magnetization of nanoscale elements using electric currents.

3. Experimental Techniques

3.1 Introduction

This chapter presents a brief introduction to the analytical calculations and the characterization techniques. Explaining how the current-induced spin torques act on the magnetization, a single (/macro) spin model implements the condition of our device and experiments. The macro-spin model calculates the response using the analytical expression of the device's ferromagnetic resonance with both applied RF and DC

current and the magneto transport measurements (DC current). An overview of the experimental set-up in TRSKM and equipment used for different configurations used to study these samples. Beginning with optical ferromagnetic resonance (FMR), which is an experimental approach to obtain the dynamic response (ST-FMR) from spintronic devices. The magnetoresistance, it is possible to electrically observe the change in magnetic states applying DC current excitation. Furthermore, the next experiment configuration is investigating the polar MOKE response under the applied step function current pulse. This approach excites only the DC SOT and DC Oe-field response from the device. Within some measurement techniques, it was necessary to employ simulations to aid the interpretation of TRSKM observations. While not the focus of this thesis, the simulation of magnetisation dynamics within spintronic devices is non-trivial and hence the methodology employed has been outlined.

3.2 Analytical macro-spin expression

This section describes the mathematical formalization of the magnetization dynamics as a single spin. The previous chapter described the mechanics of the ferromagnetic resonance (FMR) under applied DC and/or AC magnetic fields. Likewise, it is a possibility to excite the FMR with spin current by means of spin angular momentum transfer [30,49,50]. However, the Oersted field is strongly present in these applications, because they require large charge currents to generate observable spin polarized currents. The spin current will act on the magnetic damping of the precessing magnetization. The equation of motion for the magnetization precession will include both spin torque and Oersted field. The equation form of the Lifthitz-Landau-Gilbert is given as

$$\begin{aligned} \frac{d\hat{s}_{free}}{dt} = & \gamma (\hat{s}_{free} \times \mathbf{H}_{eff}) + \alpha \left(\hat{s}_{free} \times \frac{d\hat{s}_{free}}{dt} \right) + \gamma ST J \hat{s}_{free} \times (\hat{s}_{free} \times \hat{\sigma}) \\ & + \gamma FT J \hat{s}_{free} \times \hat{\sigma} \end{aligned} \quad (3.1)$$

where \hat{s} and $\hat{\sigma}$ are unit vectors of the magnetization and injected spin polarization, respectively. J is the total current density. ST and FT are the amplitudes of the Slonczewski and field-like torque terms respectively. The constant $\gamma = g\mu_B/\hbar$ is the gyromagnetic ratio, in which g is the spectroscopic splitting factor, μ_B is the Bohr magneton (and has a negative sign), and \hbar is the (reduced) Planck's constant (divided by 2π). \mathbf{H}_{eff} represents the effective magnetic field and includes contributions from the applied in-plane magnetic field, the uniaxial shape anisotropy field, the demagnetizing field, and the Oe-fields generated by the DC and RF currents passing through the device.

The calculations consider the quasi-alignment of the magnetization with the applied field to provide an accurate description on the measurement system. The realistic material systems will present a magnetization vector not fully aligned to a preferred axis; this is because the energy minimum in a material structure might not be along a

specific axis and cants on an angle from the preferred axis. As in this case, the uniaxial anisotropy field shifts the magnetization comparable to the applied field values. Instead, the orientation of the equilibrium magnetization was determined from the solution of the time-independent part of Eq. (3.1) after linearization. It was, therefore, not possible to obtain explicit expressions for the linewidth of the field swept resonance. Further details of the macro-spin model are presented in the supplementary materials in P. S.Keatley et.al. [31]

The starting point is the work presented in A.A. Tularpurkar et.al. [30], a trilayer structure like a spin valve. It consists of a fixed layer with an orientation to \hat{s}_{pin} and free layer with orientation \hat{s}_{free} . The sample is oriented at the x-z plane with the y-axis normal to the plane. Consider this in the LLG equation, introduce anti-damping and field-like STT terms and the equation takes form

$$\frac{d\hat{s}}{dt} = \gamma (\hat{s} \times H_{eff}) + \alpha \left(s \times \frac{d\hat{s}}{dt} \right) + \gamma STJ \hat{s} \times (\hat{s} \times \hat{\sigma}) + \gamma FTJ \times \hat{\sigma} \quad (3.2)$$

where t represents time, γ the gyromagnetic ratio, α the Gilbert damping constant, J the current density, ST and FT the amplitude of anti-damping and field-like STT respectively. H_{eff} is the total effective field acting upon the magnetisation, which can be written as

$$H_{eff} = H_{ext} - H_c(\hat{e}_x \cdot \hat{s}_{free})\hat{e}_x - H_d(\hat{e}_y \cdot \hat{s}_{free})\hat{e}_y \quad (3.3)$$

where H_{ext} is the static applied field, H_d is the out-of-plane demagnetising field, H_c is the anisotropic field where under the condition of our system is equal to the coercive field, $H_d = 4\pi M$ is the demagnetizing field and h_{Oe} is the local Oersted field generated by the current.

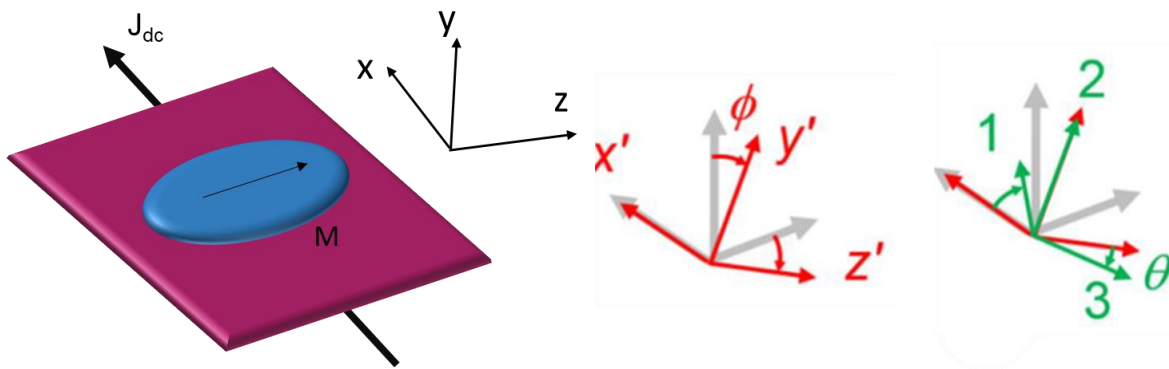


Figure 3.1: Sketch of the orientation of single spin model and lab orientation system. The DC current is flowing perpendicular to the in-plane magnetization. The unit vectors in the 2 coordinate systems are related by multiplying together matrices that represent the rotations shown above, with the results in eq. (3.7-8), and repeated here as the starting point for the more general solution (I will need to re do one of my one or use from past presentation).

We consider the specific case of the ellipsoid samples (fig. 3.1) and relate the coordinates in the lab frame to those defined by the precessing magnetization. The static magnetic field H is applied in-plane and so will have non-zero components H_x

and H_z . The current is parallel to the x-axis and the equation will include both DC and AC contributions

$$I = I_{DC} + I_{AC}e^{-i2\pi ft}. \quad (3.4)$$

The angles θ and φ define the orientation of the static magnetization

$$\hat{s}_{free}^0 = \hat{e}_1 = \cos\theta e_x - \sin\theta \sin\varphi e_y + \sin\theta \cos\varphi e_z \quad (3.5)$$

while the dynamic magnetization is given by

$$\hat{s}_{free} = \hat{e}_1 + e^{i2\pi ft}(a\hat{e}_2 + b\hat{e}_3) \quad (3.6)$$

We will focus only on the y-component, obtained by the polar MOKE response. Now we need expressions for the angles θ and φ and the precession amplitudes a and b . The angles are obtained by solving the equations

$$0 = FTI_{dc}\sin\theta - [-\sin\theta H_x - \cos\theta \sin\varphi H_y + \cos\theta \cos\varphi H_z + H_c \sin\theta \cos\theta - H_d \sin\theta \cos\theta \sin^2\varphi] \quad (3.7)$$

$$0 = STI_{dc}\sin\theta + [\cos\varphi H_y + \sin\varphi H_z + \sin\varphi \cos\varphi H_d] \quad (3.8)$$

then

$$\begin{pmatrix} a \\ b \end{pmatrix} = \frac{-1}{f_0^2 - f^2 + if\Delta} \begin{pmatrix} if - f_{22} & f_{12} - ifa \\ f_{21} + ifa & if - f_{11} \end{pmatrix} \times \begin{pmatrix} -\gamma'(-\sin\theta h_{0x} - \cos\theta \sin\varphi h_{0y} + \cos\theta \cos\varphi h_{0z} + FT\gamma'I_{dc}\sin\theta) \\ \gamma'(\cos\varphi h_{0y} + \sin\varphi h_{0z}) + ST\gamma'I_{dc}\sin\theta \end{pmatrix} \quad (3.9)$$

Where we define the paramaters

$$f_{11} = \gamma'[-H_d \cos\theta \sin\varphi + STI_{dc} \cos\theta] \quad (3.10)$$

$$f_{12} = \gamma'[H_x \cos\theta - H_y \sin\theta \sin\varphi + H_z \sin\theta \cos\varphi - H_c \cos^2\theta + H_d \cos^2\theta \sin^2\varphi + FTI_{dc} \cos\theta] \quad (3.11)$$

$$f_{21} = \gamma'[-H_x \cos\theta + H_y \sin\theta \sin\varphi - H_z \sin\theta \cos\varphi + H_c \cos^2\theta + H_d(\sin^2\theta \sin^2\varphi - \cos^2\varphi) - FTI_{dc} \cos\theta] \quad (3.12)$$

$$f_{22} = \gamma'[H_d \cos\theta \sin\varphi \cos\varphi + STI_{dc} \cos\theta] \quad (3.13)$$

We define the reduced gyromagnetic ratio as $\gamma' = \frac{\gamma}{2\pi}$

The expressions for the resonance frequency f_0 and frequency linewidth Δ are then

$$f_0^2 = f_{11}f_{22} - f_{21}f_{12}$$

$$f_0^2 = \gamma' \{ [-H_d \cos\theta \sin\varphi \cos\varphi + STI_{dc} \cos\theta] \times [H_d \cos\theta \sin\varphi \cos\varphi + STI_{dc} \cos\theta] - [-H_x \cos\theta + H_y \sin\theta \sin\varphi - H_z \sin\theta \cos\varphi + H_c \cos^2\theta + H_d(\sin^2\theta \sin^2\varphi - \cos^2\varphi) - FTI_{dc} \cos\theta] \times [H_x \cos\theta -$$

$$\left. \begin{aligned} &H_y \sin\theta \sin\varphi + H_z \sin\theta \cos\varphi - H_c \cos 2\theta + H_d \cos 2\theta \sin^2 \varphi + \\ &FTI_{dc} \cos\theta \end{aligned} \right\} \quad (3.14)$$

and

$$\begin{aligned} \Delta &= a((f_{21} - f_{12}) - f_{11} - f_{22}) \\ \Delta &= \gamma' \left\{ a \left[\begin{aligned} &2(-H_x \cos\theta + H_y \sin\theta \sin\varphi - H_z \sin\theta \cos\varphi) \\ &+ H_c (\cos^2 \theta + \cos 2\theta) \\ &+ H_d (\sin^2 \theta \sin^2 \varphi - \cos^2 \varphi - \cos 2\theta \sin^2 \varphi) - 2FTI_{dc} \cos\theta \end{aligned} \right] - \right. \\ &\left. 2STI_{dc} \cos\theta \right\}. \end{aligned} \quad (3.15)$$

The above expression for Δ is valid only for field-swept measurements considered a low field regime because the consideration of the orientation of the equilibrium magnetization changes with the field. For calculating the magnetization orientation angle (θ, φ) for each magnetic field angle, it was used a more abrupt step method as it depends on the values of magnetic field values during the field sweep. The explicit expressions for the amplitudes a and b were used for determining the out-of-plane component of the magnetization and comparing our calculation with experiments.

In the experiment, the quadrupole magnet only applies in-plane field along xz plane with a step change of values and settle time about 0.5 msec. The Oersted field is induced by current and in our configuration, it is straightforward to argue that the Oe-field components along y- and z-axis are $h_{0y}=h_{0z}=0$. The AC Oersted field h_{0x} can be calculated from the Karlqvist formula. However, these equations can be further simplified to evaluate the angles θ and φ , either when the field is applied along a high symmetry direction, or if the magnetization is quasi-aligned with an applied field. These are considered simplified solutions for a static problem.

Consider of an ideal in-plane magnetic field and no applied current setting $H_y=I_{dc}=H_c=0$, as external field H is sufficiently large that M but also parallel H . In fact, this case is only likely to be realized if H lies in the plane of the film (no competition with the demagnetization field), H_c the in-plane anisotropy field is small, and the dc spin torque is small, then the static equations

$$0 = FTI_{dc} \sin\theta - [-\sin\theta H_x - \cos\theta \sin\varphi H_y + \cos\theta \cos\varphi H_z + H_c \sin\theta \cos\theta - H_d \sin\theta \cos\theta \sin^2 \varphi] \quad (3.16)$$

$$0 = STI_{dc} \sin\theta + [\cos\varphi H_y + \sin\varphi H_z + \sin\varphi \cos\varphi H_d] \quad (3.17)$$

And the reduce to

$$0 = [+ \sin\theta H_x - \cos\theta \cos\varphi H_z + H_d \sin\theta \cos\theta \sin^2 \varphi] \quad (3.18)$$

$$0 = [\sin\varphi H_z + \sin\varphi \cos\varphi H_d] \quad (3.19)$$

Thus, for this model, the second equation has a reasonable solution is $\varphi = 0$. The static magnetization lies in plane, the first equation

$$0 = \sin \theta H_x - \cos \theta H_z \rightarrow \tan \theta = H_z / H_x \quad (3.20)$$

$$\theta = \theta_H \text{ if } H_z = H \sin \theta_H \text{ and } H_x = H \cos \theta_H \quad (3.21)$$

A similar case, as the above, but now we consider a small angle misalignment between the vectors \mathbf{M} and \mathbf{H}_{ext} , small enough so the static equations can be linearised and the calculation can be included the small DC that cants the \mathbf{M} away from \mathbf{H}_{ext} direction. Additionally, it will require conditions $STI_{dc} \ll H_d$, $H_y = 0$, and $H \gg H_c$. The final assumption may not be very realistic due to the low frequency in measurement ($f_{\text{RF}} = 2.3 \text{ GHz}$) and hence the small static field required to achieve the resonance condition. We may then write $\theta = \theta_H + \Delta\theta$ and $\varphi = \varphi_H + \Delta\phi$ where $\varphi_H = 0$, $\Delta\theta, \Delta\phi \ll 1$. Then the static equations

$$\Delta\theta = -\frac{FTI_{dc} \sin \theta_H - H_c \sin \theta_H \cos \theta_H}{FTI_{dc} \sin \theta_H \cos \theta_H - H - H_c \cos 2\theta_H} \quad (3.22)$$

$$\Delta\phi = -\frac{STI_{dc} \sin \theta_H + STI_{dc} \cos \theta_H \Delta\theta}{(H + H_d) \sin \theta_H} \quad (3.23)$$

The eq. (3.22) and (3.23) and (3.9) allow us to calculate the electrical and optical STT-FMR spectra directly.

The last thing the analytical expression can give us, it is the expression for the out of plane component m_y so we solve equations (3.22-23) with the assumption that the ϕ is small as the out-of-plane deflection angle. The out of plane deflection for magnetization is $m_y = \mathbf{M} \hat{s}_{free} \cdot \hat{e}_y = -M \sin \theta \sin \varphi$ for a small angle $\sin \varphi \approx \varphi$ we get the solution in three regions.

$$\frac{m_y}{M_{sat}} = -\frac{STI_{dc}}{H_c - H_d}, \quad H_z < H_c \quad (3.24)$$

$$\frac{m_y}{M_{sat}} = \frac{STI_{dc} H_z}{H_c (H_c - H_d)}, \quad H_c < H_z < -H_c \quad (3.25)$$

$$\frac{m_y}{M_{sat}} = \frac{STI_{dc}}{H_c + H_d}, \quad -H_c < H_z \quad (3.26)$$

The above equation, we assumed that the FT value is significantly smaller than the value of the H_z, H_d thus we consider it as $FT=0$. It is obvious from the equations that the maximum value of the m_y is linearly dependent to the ST value. This maximum magnetisation value is only dependent on the STI_{dc} product. This is not unexpected as the only effective magnetic field that can push the magnetisation out-of-plane is the ST . This corresponds to a very small value for the m_y , as it is expected since it is working against the H_d . Such small deflections may quite easily be detected by magneto-optical Kerr effect (MOKE) microscopy.

3.3 Magneto Transport technique

The magneto-resistive properties can be characterized by means electrical set-ups to determine the magnetic states of the sample. These techniques allow a rapid characterization of devices with the optical probe/set-up. However, setup may vary we present a simple schematic in figure 3.2. The source and measurement of are carried out from interconnected Keithley (Keithley 6221 current source) and nano-voltmeter (Keithley 2182A).

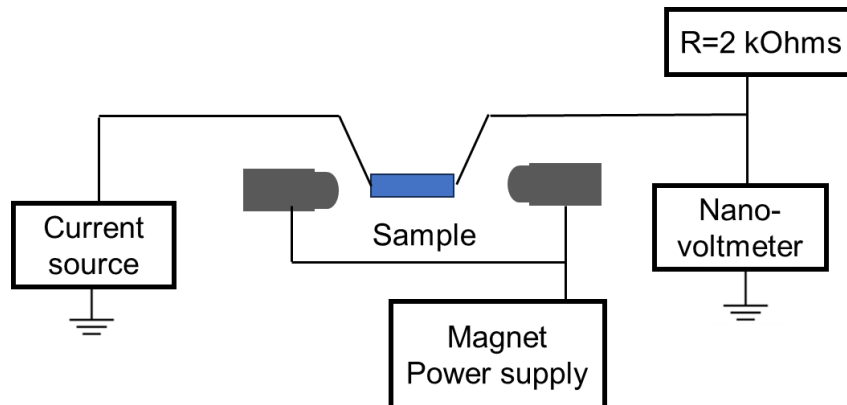


Figure 3.2: The schematics of Transport Hall measurement set-up with the two Keithley devices interconnected. The resistance of two (2) kOhms connected parallel to the device and voltmeter to avoid damaging the device. The electrical probes are landed on either side of the device on gold leads.

The Keithley nano-voltmeter is connected in parallel with a 2 kOhms resistance parallel and to the electrical Hall probes. This was introduced to the set-up to absorb the backward current signal and preserving the sample from damages. The field scan was performed by a quadrupole electromagnet with two power supplies to generate the bias field of the magnitude and orientation selected.

3.4 Time-resolved scanning Kerr measurement technique

We have described the basics of the Magneto-Optical Kerr effect (MOKE) in the previous chapter (2.2). Here we present how is implemented to develop the Time-resolved scanning Kerr microscope (TRSKM) with pulse laser and current pulse excitation. Leading the way that investigates the magnetic phenomena while the temporal resolution will be limited by the laser pulse width. Placing the sample on a scanning stage enables the investigation locally by probing the MO Kerr signal, where the limitation arises primarily from the size of the focused beam. An experimental set-up with these specifications is designed to measure the MOKE response in the macro-sized spintronics device. [31] The experimental set-up includes many optical components, to steer the beam from the pulsed laser and polarized detector to detect the change of the magnetization from the sample. A pump DPSS laser (Millennia eV) with 5 W continuous wave beam at 532 nm that is directed into the laser oscillator (Tsunami) with Ti:Sapphire crystal, produces light at 800 nm with a pulse below 100 fs. The (optical) Kerr effect (this is not the same as the magneto-optical Kerr effect) is utilized to mode lock within the gain medium inside the Tsunami's cavity. Thus, the

desired pulsed mode is transmitted in the optical path. The pulsed frequency is synchronized from an external source at 80 MHz by use of a piezoelectric motor to adjust the separation of the laser's cavities mirrors.

A power meter is placed to monitor the laser beam intensity, we can adjust the cavity mirrors by monitoring the output power. A half-wave plate and a beam splitter (90:10) are used to adjust the intensity between the sample path and towards the power meter. In the main sample path, the laser beam directed through a second harmonic generator crystal, this reduces the intensity of the 800 nm beam but converted to a blue beam (400 nm). The beam is directed into a retro-reflector mounted on a translational stage, which acts as a delay line with a maximum delay of 4 ns which is used for time-resolved measurements. A residual (800nm) beam was noticed in the 'sample path', however, after placing a bandpass filter is negligible.

The beam is passed through a beam expander and half-wave plate, the beam is reconfigured before entering the microscope setup. As the beam entering the microscope, a periscope set of mirrors to direct the beam to a perpendicular direction going towards the sample. The beam passes through a linear polarizer (Glan Thompson crystal) to ensure its linear polarization. An uncoated beam-splitter is before the objective lens x50 of long working distance (NA=0.6) where the beam is focused on the sample to diffraction limited spot of 400 nm. A beam splitter effectively directs the reflected light towards the balanced detector, which comprised of a beam splitter and two photodiodes. The incident light upon the detector undergoes a division by the beam splitter, segregating it into mutually perpendicular polarization components, subsequently aligning each resultant beam onto a respective photodiode.

It is feasible with this configuration to selectively detect the components of the magnetisation. In our experiment, the polar configuration is used to detect the MOKE signal from the out-of-plane component of the magnetization. Additionally, the MO longitudinal Kerr signal (fig. 2.2) can be detected indirectly and is related to the in-plane component of the magnetization. What we measure with longitudinal is the precession motion of the magnetization along the plane of the incident which often refers to the s-component. In contrast, the transverse configuration is generally measured from the changes in the intensity of the reflected beam. Those intensity changes in our experiment are linked to the "p" component magnetization.

The magneto-optical studies are polarimetry measurements with a fixed optical wavelength and the changes in polarization are directly proportional to the magnetic response. In such systems, the parameters e.g. temperature, film thickness can be varied while critical phenomena, magnetic anisotropy can be studied. Highly sensitivity probes are designed to investigate these small changes in ellipticity and rotation of laser beam's polarization.

MOKE probes samples over a depth which is the penetration depth of light. In the case of metallic multilayer structures (most of the samples treated in this work), the penetration depth is about 20 nm. Thus, compared to integral techniques (e.g. SQUID or sample vibrating magnetometer), MOKE could be considered as a surface sensitive technique, which has been claimed by several authors who even called it Surface

MOKE (SMOKE). MOKE is considered as a magnetic in-depth sensitive technique allowing to study buried FM layers.

3.5 Excitation of spin dynamics driven by DC and RF current to observe DC SOT

Spin dynamics can be excited by electric excitation of different form depending on the physical limitations of the sample and the experiment. The setup we discussed here are prototype to investigate the magnetic response of device like the SOT magnetic tunnel junction. The pump-probe technique it is used to synchronising of the driven dynamics and the laser repetition rate.

This configuration is used for a ferromagnetic resonance experiment. This investigation can be generally used on spintronics devices through the same principles apply to other experiments. The main components that are in the optical path of the laser beam are shown in the figure 3.3 and the electric equipment for generated the DC and RF current that functions as the excitation pulse. The synchronisation between the RF current generator and the laser pulses is achieved by connecting both with a master clock. The Atlantec low phase noise oscillation instrument supplies with an RF signal at 80 MHz both the Tsunami laser oscillator and microwave synthesizer, thus both are locked to this frequency signal. Then, the RF current generator produces the RF injected current at the frequency and amplitude determined by the magneto-transport methods to achieve to spin-injection locking (or phase locking). The magneto-transport field scans are employed to determinate the amplitude of electrical current and the saturation magnetic field value to achieve synchronisation.

For the experimental measurements, we apply an in-plane magnetic field at angle from the easy axis of the ellipsoid, thus aligning the magnetisation along the desired direction. A microwave signal at a fixed frequency is passed through the sample, while the amplitude of the external magnetic field was allowed to vary. The optical ST-FMR technique does not require any external RF field, as the injected RF current signal produces the (AC) spin-orbit torque needed to excite the ferromagnetic resonance in the magnetic layer. While a bias-tee separates the AC and DC currents where a change in DC voltage at the modulation frequency can be detected by a lock-in amplifier. An additional current source can be used as a DC bias current for investigations of spin torque. [49] This technique can compare the FMR response and field scan curve as it is useful to obtain material parameters, and hence is of significance in the characterisation of spintronic device. [51,52]

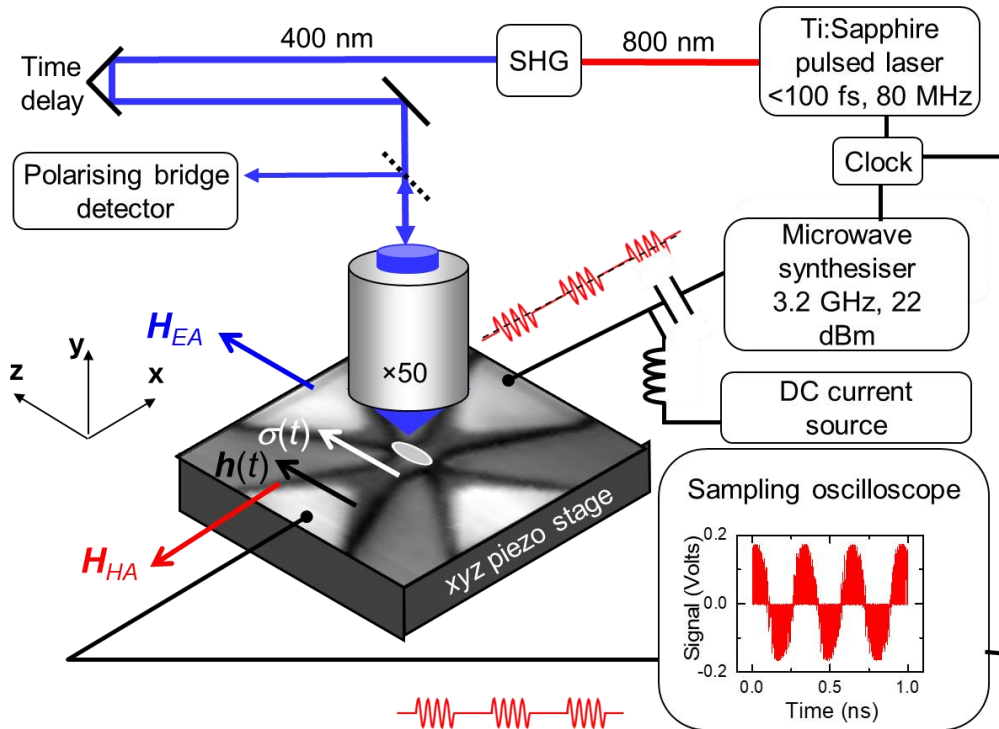


Figure 3.3: Schematics of the experimental ST-FMR setup for the SOT-devices. (a) Optically detected, phase-resolved SOT-FMR in a TRSKM. Ultrafast laser pulses with a duration $<100\text{ fs}$, a repetition rate of 80 MHz, and a wavelength of 800 nm are converted to a wavelength of 400 nm by SHG. The pulses are synchronized with the GHz-frequency RF output of a microwave synthesiser. The phase of the RF waveform was monitored using a sampling oscilloscope (inset, measured waveform showing amplitude modulation). RF and DC currents were passed to the device simultaneously via a bias tee, high frequency microscale coaxial probes, and the wider ($2\text{ }\mu\text{m}$) current lead of the Pt Hall cross. The width of the current lead was approximately equal to the length of the long, EA of the ellipse, which was perpendicular to the current direction. The resulting Oe-field $\mathbf{h}(t)$ and injected spin polarization $\sigma(t)$ at the Pt/CoFeB interface were, hence, parallel to the EA, from which the in-plane applied field H angle θ_H is also defined.

Throughout this chapter, we describe optical ST-FMR technique used in TRSKM microscope. The optical technique is a power tool to characterize these devices where it can probe the spatial response and local effects, in contrast to its electrical counterparts. As discussed in the previous chapter, FMR technique is a tool to characterize the different ferromagnetic layered stacks. In chapter 4, the discussion of results of measurements from optical ST-FMR in TRSKM. Moreover, it is included a presentation of the derivation of analytical expressions for the resonance curves of the out of plane component of magnetisation. The derivations of these equations are presented below.

3.5 Observing the magnetization dynamics with bi-polar pulse

This experiment configuration is designed to demonstrate the response of DC SOT by applying a square wave pulse at a frequency of 3.14 kHz. The step function current pulse excites a semi-static state of magnetization that is similar to a static measurement. Therefore, this called quasi static MO Kerr measurement. The optical

probing is pulsed laser is focused with a 400 nm width beam on the perpendicular direction of the sample. This is a stroboscopic approach to the experiment where, simultaneously, the current pulse come from electrical probes parallel to the narrow axis of the sample.

The sample is positioned on top of a piezoelectric controlled stage, where is located the (geometric) center of the quadrupole magnet. The magnetic field is homogeneous, and the generated field can be swept and vary at different directions along the x-z plane (in-plane). The piezo-controlled stage is used to spatially scan over the device. This configuration is recorded the corresponding polar Kerr rotation and the reflectivity of the device. It is important to generate an image scan of the device before each field scan, so the beam probe will be direct from the centre of the ellipse. The size of the ellipse in the devices presented here is $1000 \times 400 \text{ nm}^2$, which close to the beam spatial resolution $\sim 400 \text{ nm}$. In figure 3.4, on top of the xyz piezoelectric stage, there is a greyscale image of the device as extracted from a zero field imaging scan. The high reflectivity region shows the ellipsoid and gold leads. The ellipsoid has been highlighted with an overlaid ellipse graphic.

A transport Hall effect (THE) measurement was performed to determine the coercive field value H_c for this device with respect to the applied field along the HA-axis. A theoretical value from the analytical expression

$$V_x \propto \frac{H_z}{H_c} \sqrt{1 - \left(\frac{H}{H_c}\right)^2} \quad (3.18)$$

which can help estimate the H_c (coercivity field) and be confirmed from the magneto-transport measurements. After we have characterised the sample with these electrical measurements, we carry on with the magneto-optical study. The experimental setup may be seen in fig. 3.4.

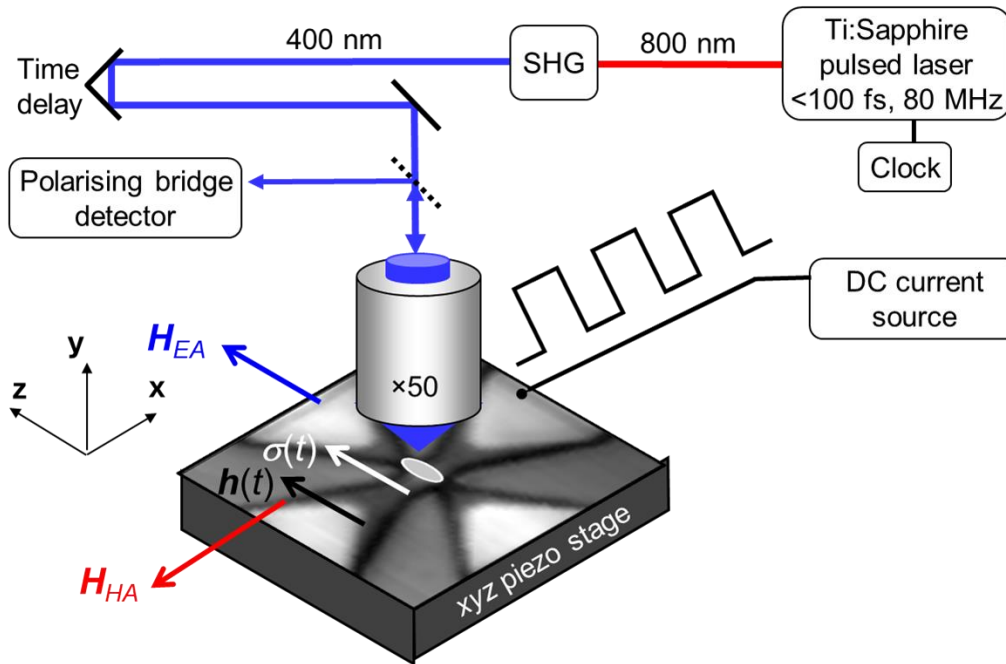


Figure 3.4: The schematics of experimental set-up for the quasi-static configuration. The square-wave current pulsed is directed parallel to the narrow axis of the ellipse (highlighted shape) so the induced Oersted field $h(t)$ parallel to the spin polarization $\sigma(t)$. The sample is shown from an image scan on top of the xyz piezoelectric stage. The gold leads begin at the edge of the Platinum Hall cross edges. The beam from the Ti:Sapphire laser is converted to a 400 nm light with a second harmonic generation crystal. The probing beam is directed on the sample from the perpendicular direction and the reflected beam is detected from a polarizing bridge detector with the introduction of a beam splitter.

The spatial resolution provided by our magneto-optical technique has allowed us to closely monitor the evolution of the out-of-plane magnetisation deflection. The optical beam probe is similar to the previous section. The function generator is also connected with the lock-in amplifier tune the MOKE response we detect with the excitation frequency. The reflected beam from the sample response is directed to the detector. There, the reflected light is analysed in a polarizing beamsplitter (PBS) and two photodiodes. The signal is amplified by a differential amplifier. The MOKE response is separated to the two diode's signal (or DC and AC MOKE signal). We correctly phase-optimized the lock-in amplifier, the real MOKE signal is measured. The polar MOKE response in this in-plane magnetized sample will be only current-induced. This has allowed us to perhaps disentangle one of the effects that may have contributed to the wide range of reported values for the spin-orbit-torques. [50,51]

In contrast to the benefits of TRSKM approach, the downsides originated as a result of the long acquisition times, as effect of sample drift and noise. Additionally, the optical components heating up and shifting over time can result in changes in laser intensity due to beam drift, and sample drift can lead to disjointed or blurred scanned images. Furthermore, sources of optical noise can lower the system sensitivity and disrupt the imaging process. Despite these drawbacks TRSKM has become a powerful tool for observing the magnetization dynamics. This technique has long been used for aiding the development of read/write devices for magnetic storage [53,54] as well as investigating dynamics in a variety of magnetic nanostructures, [55] and the Spin Hall Effect. [33]

4.Observation of Spin-orbit torque induced ferromagnetic resonance

Magnetic tunnelling junction (MTJ) has been a common device for STT investigation on phenomena such as spin accumulation [56–58] and spin pumping [58–60]. The Spin Hall Effect [37,39,62,63] has gained interest in bilayer structures HM/FM due to the potential application in magneto-resistive random access memory (MRAM). A different approach to STT-MTJ is the Spin Orbit Torque - MTJ where the current is applied in-plane along the heavy metal (HM), and with the advantage of the SHE implementation, reduces the device size, it improves energy efficiency and increases device longevity.

One way to detect the SOT response is from ferromagnetic resonance techniques using a phase-resolved configuration in the Time-Resolved Scanning Kerr microscope (TRSKM). This optical technique is better at detecting the local magnetization components, rather than its electrical counterparts, which measures the spatial average orientation of the magnetization by performing magnetoresistance or Hall effect measurements. Those measurements provide a transverse voltage difference of the device, while the magnetic field is swept, but the phase of the dynamic response cannot be determined.

In-plane magnetized elements could present non-uniform equilibrium states, that have been named leaf, S- and C-shape states. [63] In those elements magnetization cants along the edges of the element and is not fully aligned parallel to the direction of the applied magnetic field. In in-plane magnetized SOT devices, the interface between a heavy metal/ferromagnet can convert the charge current passing through the heavy metal to a pure spin current by means of the Spin Hall effect (SHE). The SOT acts on the magnetization as it precesses along the orientation of the applied magnetic field. The detection of out-of-plane component is observed by the ellipticity, or rotation of the polarization reflected beam, which is proportional to the magnetization changes, while the magnetic field is swept.

In this chapter, an ellipsoid thin-film element was subjected to the Oersted (Oe) field and SOT, generated by simultaneously injecting an RF current (I_{RF}) and a DC current (I_{DC}) into the device. Field swept SOT-FMR spectra were recorded at the centre of the ellipse so that the centre mode could be utilized as a probe of the SOTs, thus avoiding non-uniform edge effects. [31] The complex signal is used to determine the spin torques that act on the magnetization, by analysing the resonance field and linewidth. [37,50,65] The analysis focuses on the attributes like the resonance field, or frequency, and linewidth allows the magnitude of the spin torques acting upon the magnetisation to be determined. [4,30,37,49,50,65–68] The dependence of the optically detected spectra on the orientation of the in-plane applied field was well reproduced by a macrospin model, allowing the values of both the damping parameter and the SOT parameter to be determined.

The conventional electrical ST-FMR is a widely used characterization technique in spintronics. Radio frequency (RF) current is injected with an audio frequency

modulation to excite the magnetisation, and combined with the Magnetoresistance (MR) response, the device generates a DC mixed voltage (V_{mix}) signal, which is recorded as the applied magnetic field, or the frequency of the current is varied. In previous work with spin Hall nano-oscillators (SHNO) [64], where the SHNO was examined with electrical ST-FMR technique, it was observed that the symmetry of the MR mechanism, the V_{mix} vanishes for specific magnetic field orientations, and a spatial average of magnetisation dynamics is presented that it might be a highly inhomogeneous device/element. While further research has been conducted with this optical SOT-FMR technique in spin Hall nano-oscillator devices the characterization of only the torque generated by RF current. [36,51,52]

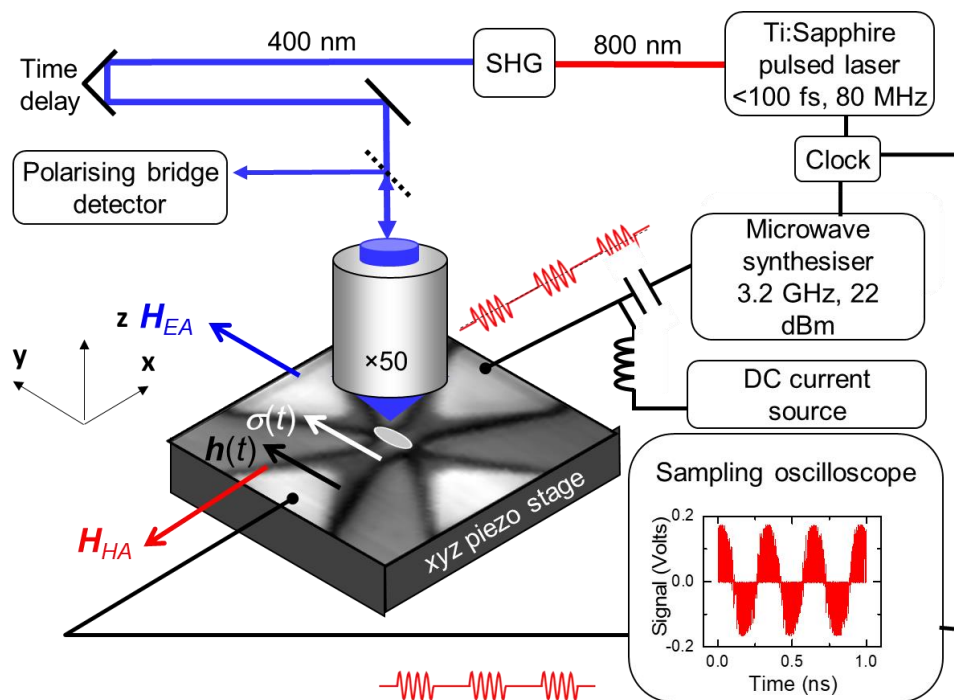


Figure 4.1: The schematics of TRSKM. Optically detected, phase-resolved SOT-FMR in a TRSKM. Ultrafast laser pulses with a duration $<100\text{ fs}$, a repetition rate of 80 MHz, and a wavelength of 800 nm are converted to a wavelength of 400 nm by SHG. The pulses are synchronized with the GHz-frequency RF output of a microwave synthesizer. The phase of the RF waveform was monitored using a sampling oscilloscope (inset, measured waveform showing amplitude modulation). RF and DC currents were passed to the device simultaneously via a bias tee, high frequency microscale coaxial probes, and the wider ($2\text{ }\mu\text{m}$) current lead of the Pt Hall cross. The width of the current lead was approximately equal to the length of the long, EA of the ellipse, which was perpendicular to the current direction. The resulting Oe-field $h(t)$ and injected spin polarization $\sigma(t)$ at the Pt/CoFeB interface were, hence, parallel to the EA, from which the in-plane applied field H_{θ} is also defined.

The Fig. 4.1 shows the TRSKM for the ferromagnetic resonance configuration. The RF current was generated by a microwave synthesiser with an RF power of 22 dBm and frequency of 3.2 GHz = $n \times 80\text{ MHz}$, where here is $n=40$. The synchronous repetition rate of the laser pulsing is fixed at 80 MHz. We have calculated the reflection coefficient of the device equal to ~ 0.87 , due to the transition from 50 Ohm coaxial cables and electrical probes on the device load of about 700 Ohms. The electrical probe's tips are landed on either side of the minor axis (or Hard axis-HA), so the charge current would flow perpendicular to the longer axis (Easy Axis- EA) of the ellipse. The

injected spin polarized current, and the induced in-plane component Oe-field are parallel along the EA. Thus, when we apply the magnetic field along the HA will expect the strongest amplitude of torque act on the magnetization.

The AC and DC Oe fields acting on the ellipse were calculated to be approximately 25 Oe ($I_{RF}= 8$ mA) and 30 Oe (for $I_{DC}= 10$ mA), respectively. Non-linear effects were not observed in either the measured or calculated spectra, and measurements were found to be insensitive to resonance thermal effects. [36] The RF current amplitude was modulated at $f=3.14$ kHz and the resulting modulation of the out-of-plane component of the dynamic magnetization was detected via the polar MO Kerr effect, using a balanced polarizing photodiode bridge detector and a lock-in amplifier. Amplitude modulation was used in analogy to electrical SOT-FMR measurements. [51] The DC current was generated by a precision current source and combined with the RF current using a bias tee.

Figure 4.1 shows also the layout of the device from the imaging scan, performed on the device. The fabrication details of these devices have been reported previously. [59] Magnetron sputtering was used to deposit a Pt(6)/Co₄₀Fe₄₀B₂₀(2)/MgO(1)/TaO_x(4) (thicknesses in nm) film onto a Si substrate with a SiO₂ (250 nm) thermally oxidized overlayer. The stack was then annealed, after which electron beam lithography and ion milling were used to form a Hall cross device consisting of a 2000x800 nm², CoFeB/MgO/TaO_x ellipse centered on a Pt(6nm) cross design. The Pt Hall cross was intentionally overmilled by approximately 1 nm over the perimeter of the ellipse, where the other layers are deposited. The incident beam comes perpendicular to the ellipse surface, focused by a diffraction limited objective lens with resolution of 400 nm spot.

The Tsunami laser beams are converted from 800 nm to 400 nm wavelength by means of second harmonic generation (SHG). The beam path is introduced in a 4 nsecs. delay line was used for the acquisition of the time-resolved signal; thus, we can extract accurately the phase of the probing laser pulses with respect to the 2.4 GHz 22 dBm RF current excitation that passes through the device. A bandwidth filter was placed on the beam paths to remove the residual red (800 nm) light. The power of the beam is average around 200 μ W and it is attenuated, before passing by the x50 (NA=0.55) long working distance (\sim 11 mm) objective lens. The beam path is introduced in a 4 nsec. delay line was used for the acquisition of the time-resolved signal; thus we can extract accurately the phase of the probing laser pulses with respect to the 2.4 GHz 22 dBm RF current excitation that passes through the device.

Last step to determine the approximate conditions for resonance (resonance field and frequency) is to perform preliminary time-resolved (TR) polar Kerr measurements. The TR scan uses a broadband current pulse (\sim 30 ps rise, \sim 70 ps duration) to excite the uniform mode of precession. Figure 4.2 (a) shows the precession at the centre of the 2×0.8 μ m² ellipse following the pulsed field excitation at $t=0$ ns for a applied field at about +200 Oe applied along the hard axis. The time-resolved response is a single scan (not averaged) acquired over 3 ns of time delay with a step size of 20 ps. The frequency of precession can be determined from the fast Fourier transform power spectrum (Fig.4.2 (b)) of the measured precession signal in Fig. 4.2(a). This provides the necessary information to set the in-plane magnetic field and RF frequency for a

time-resolved measurement at resonance in response to an RF current waveform. (supplementary materials in [31])

The measured response to the RF current is sinusoidal and shown in Fig. 4.2(c) for an RF frequency of 2.72 GHz and an in-plane bias magnetic field of ~ 200 Oe. The time-resolved response is a single scan (not averaged) acquired over 1 ns of time delay (approximately 3 RF cycles) with a step size of 20 ps. The time delay stage was set to a fixed position on the sinusoidal response (node (τ_1) or anti-node (τ_2) positions). When sweeping the in-plane applied magnetic field, the detector acquires the real or the imaginary component of the dynamic magnetic susceptibility for either position.

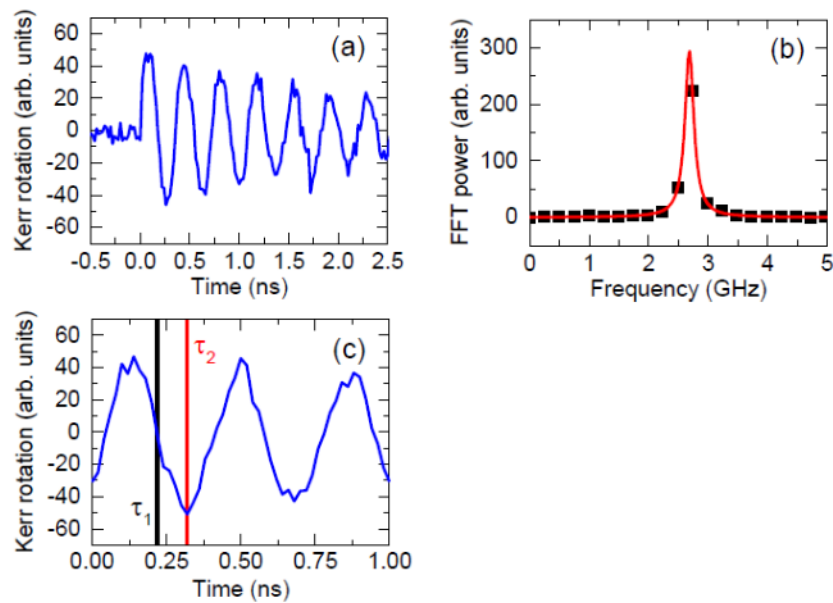


Figure 4.2: A time-resolved polar Kerr signal in response to a broadband current pulse (~ 30 ps rise, ~ 70 ps duration) is shown. An in-plane magnetic field of ~ 200 Oe was applied parallel to the hard axis of the ellipse, and perpendicular to the Oersted field generated by the current pulse. (b) A fast Fourier transform of the TR signal in (a) reveals a precession frequency of ~ 2.7 GHz. (c) A time-resolved polar Kerr signal in response to an RF current is shown for an RF frequency 2.72 GHz and in-plane field of ~ 200 Oe applied parallel to the hard axis. The RF frequency was close to the resonance frequency at ~ 200 Oe identified from the FFT in (b), but also an integer multiple of the laser repetition rate (34×80 MHz). The RF power was 20 dBm. These phase-resolved spectra were acquired by sweeping the in-plane magnetic field parallel to the hard axis when the time-delay between the RF current and the probing laser pulse was respectively set to a node (τ_1) and antinode (τ_2) of the precession signal acquired at resonance in (c). In fig. 4.3(a) and (c) the lock-in amplifier time constant was 2 s.

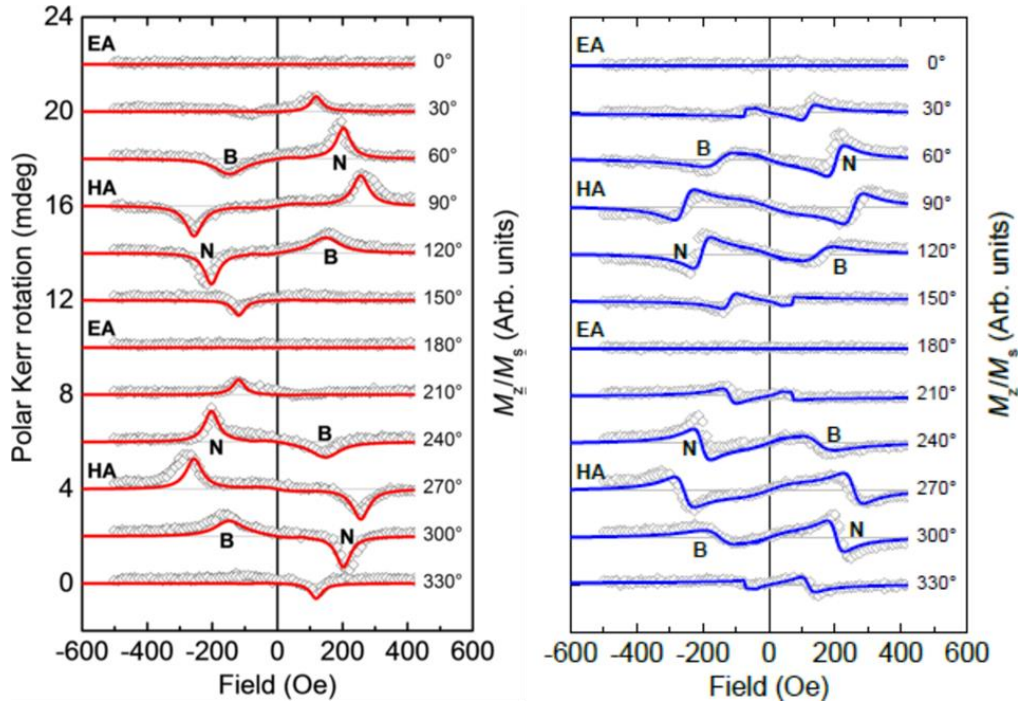


Figure 4.3: Optically detected phase-resolved SOT-FMR spectra (grey open symbols) corresponding to the (a) imaginary and (b) real component of the dynamic susceptibility and acquired over the full range of azimuthal angle Θ_H defined with respect to the EA (0°). f_{RF} and I_{DC} had values of 3.2 GHz and 10 mA respectively. Calculated spectra for a single macrospin are overlaid (red and blue curves). The calculations assumed $f_{RF} = 3.2$ GHz, $I_{DC} = 10$ mA, $I_{RF} = 8$ mA, $ST = 6.75 \times 10^{-7}$ Oe / A / cm^2 , a uniaxial anisotropy field of 90 Oe, demagnetizing field = 7500 Oe, g -factor = 2.05, $a = 0.025$, Pt lead width = 3.5 μm , and Pt thickness = 6 nm. The measured spectra are shown for both field sweep directions, while for clarity the calculated spectra are shown only for a single sweep direction (avoiding field sweep segments for which the energy minimisation routine can yield metastable equilibrium states after sweeping through remanence). The measured (calculated) spectra have been offset by 2 mdeg ($0.08 M_z/M_s$) for clarity. Example of broad and narrow FMR peaks are labelled letters B and N respectively.

For the field scans on the fig. 4.3, we have identified the respected position of the delay stage and injected RF and DC current simultaneously. A second field scan was performed, when the position of the delay stage was moved to the other position (anti-node position), repeated the measurement to probe the dispersive component. In fig. 4.3 shows the experimental spectra of the measured polar Kerr signal for different orientations of the in-plane applied magnetic field. The marco-spin calculations are shown with solid red and blue lines overlaying the experimental spectra (open cycles). The agreement with the experimental data and the calculations is a response described by a single macro-spin.

Additionally, the Kerr signal observed for the applied field aligned at the EA axis ($0^\circ, 180^\circ$) and no FMR peaks were present because no torque was exerted on the magnetization. When the current induced Oe-field and spin polarization lie parallel to the magnetization vector, there is no torque to act as the magnetization lies on the EA axis. In contrast, when the field is applied on the minor axis ($90^\circ, 270^\circ$), strong FMR peaks are observed because the Oe-field and the injected spin polarization exert the maximum torque on the magnetization. However, there is no observed asymmetry with respect to the polarity of the FMR peaks in either amplitude resonance field or linewidth. When the applied field orientation lies between the EA and HA, and for the case of $I_{DC}=10$ mA, both experimental and calculated spectra in fig. 4.3 show a marked

asymmetry in the amplitude and linewidth of the FMR peaks at positive and negative field values. At these intermediate field angles, the equilibrium magnetization has a component that lies either parallel or antiparallel to the O_e -field and spin polarization, depending on the field polarity.

This leads to either an enhancement or reduction of the effective damping and the corresponding SOT-FMR linewidth as most clearly observed in Fig. 4.3 at angles $\pm 30^\circ$ from the HA. For example, broad (B) and narrow (N) peaks are observed for $-H$ and $+H$ values at $\theta_H=60^\circ$, while B and N peaks occur for '+H' and '-H' values at 120° . Spectra calculated for $ST=0$, but including the O_e field due to the DC current (not shown), also show asymmetry in the amplitude and linewidth with respect to field polarity similar to that observed in the experiment. Therefore, the asymmetry observed in the experiment is due to the combined effect of the O_e field and SOT. Changing the HM from Pt to, e.g., W could confirm this conclusion since spin Hall angles of opposite sign are observed for these materials. [63]

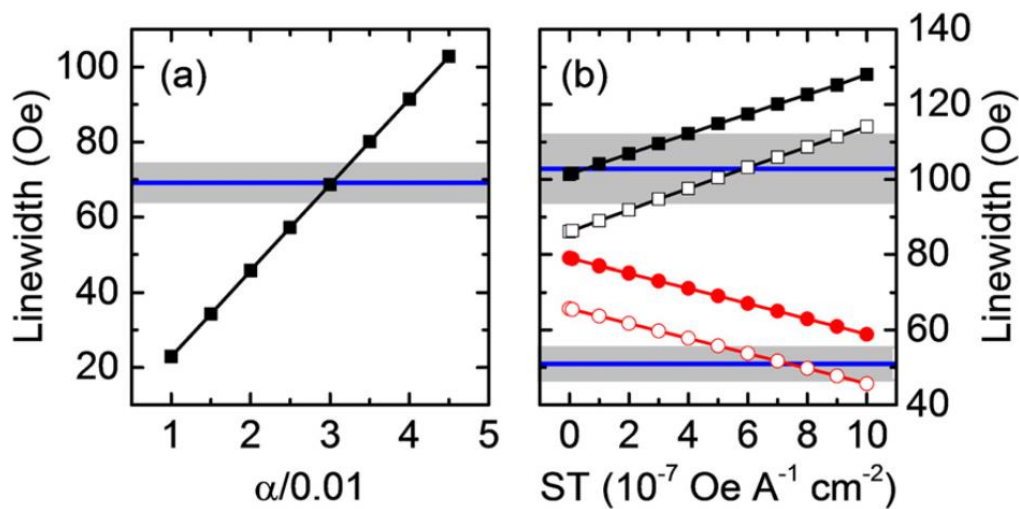


Figure 4.4: (a) Calculated HA linewidth (black squares) vs damping parameter α for $I_{DC}=0$ mA. The horizontal blue line shows the average value measured for different field histories, while the light gray band represents their standard deviation. (b) Calculated linewidth vs ST parameter for the broad (B) (black squares) and narrow (N) (red circles) peaks at '+H' and '-H', respectively, for $\theta_H=120^\circ$ and $I_{DC}=10$ mA (see Fig. 4.3). The filled (open) symbols assume $a=0.030$ ($=0.025$). Comparison is made with the linewidth determined from 8 equivalent measurements of both the B and N peaks. The blue horizontal lines indicate the average experimental linewidth values, while the light gray band represents their standard deviation.

The simulated parameters were calculated by the adjusting the parameters. At first, the value of the damping parameter α was first determined from the HA linewidth for the case of $I_{DC}=0$ mA, where the linewidths within the SOT-FMR spectra are found to be insensitive to the ST parameter. [25] The linewidth is defined as the full width at half maximum of a Lorentzian curve fitted to the peaks in the calculated and experimental SOT-FMR spectra. In figure 4.4(a) shows the linewidth of the calculated HA spectrum for different values of the damping parameter. The average linewidth determined from experimental HA spectra measured for two different field histories (horizontal blue line) agree best with the calculations for $a=0.030\pm 0.003$, compared to $a=0.035$ reported for smaller ($80\times 205 \text{ nm}^2$) devices of the same composition.

Using the value of $a=0.030$ determined from the HA measurement, spectra were first calculated for different values of ST and the B and N linewidths extracted. Figure 4.4(b) shows a clear linear increase (decrease) in the linewidth of the B (N) peaks as the ST parameter is increased from 0 to 10×10^7 Oe A/cm². Comparison is made with the 8 equivalent measurements (field swept up and down for $\theta_H=60^\circ, 120^\circ, 240^\circ,$ and 300°) of both the B and N peaks. The blue horizontal lines indicate the average of the 8 experimental linewidth values. Assuming $a=0.03$, the calculated linewidth of the B peak for $\theta_H=120^\circ$ shows best agreement with the average measured linewidth (blue line) for $ST=0.6 \times 10^7$ Oe/ A/cm². In contrast, a value of $ST > 10 \times 10^7$ Oe /A/cm² is needed to bring the calculated linewidth of the N peak in agreement with the measured values. However, if a smaller value of $a=0.025$ is assumed, good agreement between experiment and the calculation is obtained for both B and N peaks when $ST=(6.75 \pm 0.75) \times 10^7$ Oe/A/cm².

The dependence of the resonance field and linewidth on the orientation of the applied field is plotted for both positive and negative field polarities in Fig. 4.5. The variation of the resonance field can be described as the superposition of a two-fold $\sin^2(2\theta_H)$ term due to the uniaxial shape anisotropy and an one-fold $\cos^2(\theta_H)$ term due to the DC Oe field. The latter term results in a difference in the resonance field with respect to field polarity for certain angles and causes the values of the resonance field to differ between $\theta_H=60^\circ$ and 120° , whereas these values would be equivalent in the absence of the Oe field (gray arrows highlight the difference in Fig. 4.5(a)).

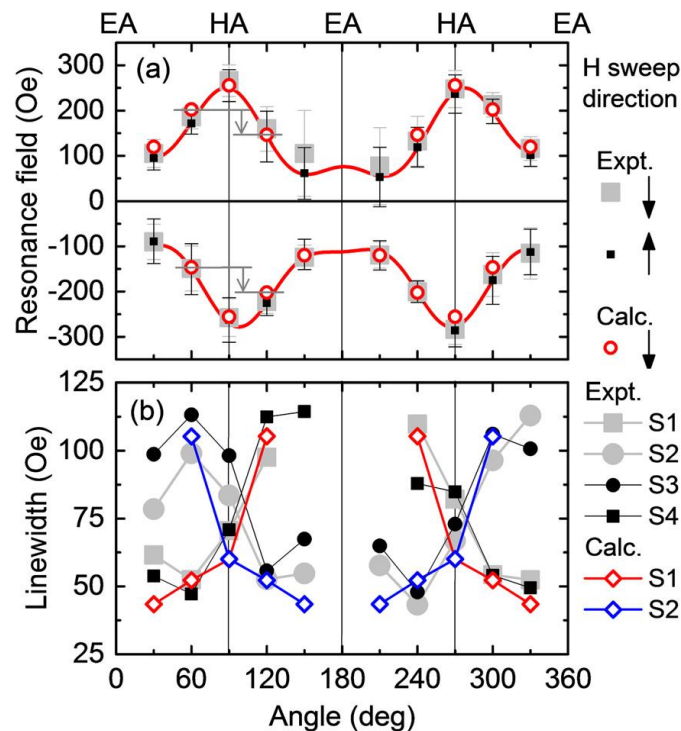


Figure 4.5: Measured resonance field vs applied field angle for $I_{DC}=10$ mA. The field was swept from positive to negative values (large filled gray squares, down arrow) and then from negative to positive (small black filled squares, up arrow). The length of the error bar indicates the measured linewidth. The resonance fields determined from the calculated spectra assuming $a=0.025$ and $ST=6.75 \times 10^7$ Oe A/ cm² are also shown (open red circles). The guide to the eye (red curves) contains $\sin^2(2\theta_H)$ and $\cos^2(\theta_H)$ terms, while the difference in the resonance field at an angle of 30° on either side of the HA ($\theta_H=90^\circ$) is shown by small gray arrows. (b) Measured linewidth vs

applied field angle (gray and black symbols), for different segments of the field sweep; positive to remanence (S1), remanence to negative (S2), negative to remanence (S3), and remanence to positive (S4). The linewidths of the calculated curves are shown for segments S1 and S2 only for clarity.

Calculated spectra (fig. 4.5) indicate that the resonance field has a negligible dependence on the ST parameter, and so to observe the influence of SOT, it is necessary to look in detail at either the amplitude or the linewidth of the observed FMR peaks. Figure 4.5(b) shows that there is a distinct crossover in the linewidth value as the field angle crosses the HA and as the component of magnetization that is collinear with the Oe field and spin polarization changes its sign. In light of the symmetry of the anisotropy and Oe fields, the spectra for $\theta_H=60^\circ$, 120° , 240° , and 300° are equivalent, each containing one B and one N peak with similar resonance fields and linewidths. It is, therefore, sufficient to compare these measured B and N linewidths with those calculated for a single field angle of $\theta_H=120^\circ$. (Fig. 4.6)

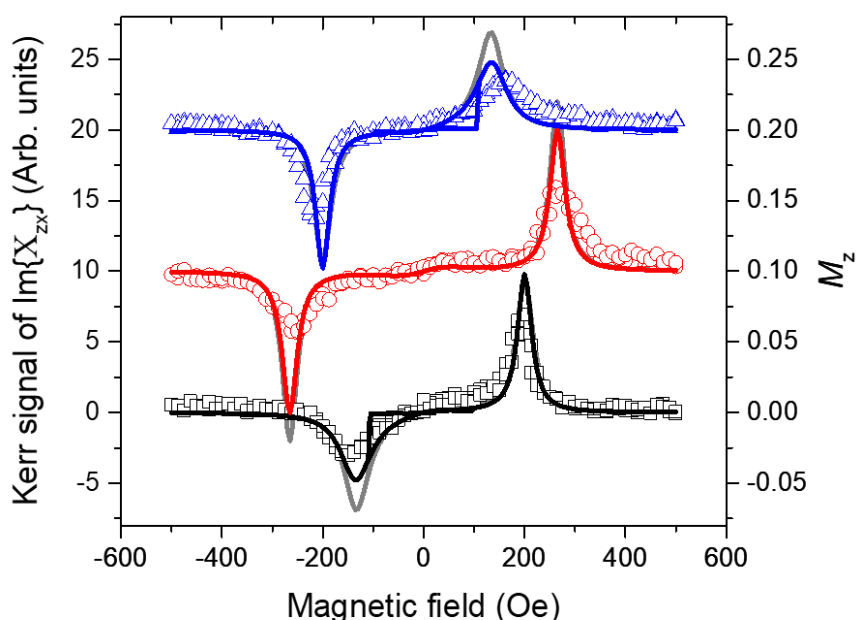


Figure 4.6: The experimental spectra (open symbols) overlaid the numerical calculation solid lines. The numerical simulation indicates that the resonance field value is insensitive to the value of ST and strongly dependent with the field angle (Here $\theta_H=120^\circ$, 90° , 60° respectively from top curve to bottom). The distinctive asymmetry of the curve shows that for simulation with ST parameter equal to zero ($ST=0$) the linewidth is effective slightly. This is also caused from the DC Oe-field still act on the magnetization. For our numerical modelling we use the following parameters for demagnetization field $H_d=7500$ Oe, the uniaxial anisotropy is $H_c=-90$ Oe, we assumed $f_{RF} = 3.2$ GHz, $I_{DC} = 10$ mA, $I_{RF} = 8$ mA. The other parameters are g-factor = 2.0, the damping constant is $a = 0.025$, the sample width is considered an effective value $w = 3.5$ nm, and the Pt thickness is $d_{Pt} = 6$ nm. The ST value was selected for the solid coloured line to be $ST = ST = 6.75 \times 10^{-7}$ Oe/A/cm² and the calculation that represented for grey solid line $ST=0$.

Our numerical simulation shown in fig.4.6, the resonance curves represent only the absorptive part. On the calculation we have chosen the Slonzcewski torque values of $ST=0 \times 10^7$ Oe/A/cm² and $ST=6.75 \times 10^7$ Oe/A/cm². The results show a slightly difference for the $ST=0$ curve meaning that our results are originated from a contribution of DC SOT and DC Oe-field. The best agreement results we obtained by some tune of the experimental parameters, such as the width of the sample to increase from 2 μm to 3,5 μm . This change is acceptable as the effective area through which the current

flows and reduces the current density and induced Oe-field at the ellipse. Additionally, the spreading of the RF current was previously reported within spin Hall nano-oscillators [8] due in part to the reactance of the device structure. It is, therefore, quite difficult to establish the current distribution within this device.

The FMR spectra were measured for a range of DC current from 0 to 10 mA. (supplementary materials of [31]) In the lower current the Kerr amplitude is reduced to 0 or 1 mA compared to 10 mA and the asymmetry is not visible because SOTs are either weak or inactive when the ellipse is magnetized along the HA. Moreover, the analysis of the HA linewidth with respect to DC current densities suggests that it is insensitive to the thermal effect in the Pt. Moreover, in [25], the angular-dependent SOT-FMR measurements performed for $I_{DC}=1\text{mA}$ do not show the marked asymmetry in amplitude and linewidth seen for measurements with $I_{DC}=10\text{ mA}$. When the field was applied parallel to the HA with $I_{DC}=1\text{ mA}$, comparison with macro-spin calculations yielded $a=0.033$, while the expected smaller, linear variation of the linewidth as a function of ST parameter was found to lie within the experimental uncertainty. The fact that the value of a decreased somewhat as I_{DC} was increased from 1mA to 10mA suggests improved spatial uniformity of the equilibrium state and rules out a significant role for thermal effects up to $I_{DC}=10\text{ mA}$. For $I_{DC}=1\text{ mA}$, the calculated dependence of the linewidth on the field orientation was found to be smaller than the experimental uncertainty, and so only the measurements made at $I_{DC}= 10\text{ mA}$ were used to determine the value of the ST parameter.

In summary, TRSKM has been used to perform optically detected, phase-resolved SOT-FMR measurements. A center localized mode was used to probe the SOTs active at the centre of a micro-sized ellipse, thus avoiding non-uniform edge effects. Macro-spin calculations reveal that a combination of both Oe-field and SOT is required to reproduce the marked asymmetry of the FMR spectra with respect to the polarity of the applied field. By comparing the measurements with the calculations, the values of the damping parameter and ST parameter can be determined, while the insensitivity of the measured HA linewidth to DC current suggests that thermal effects do not influence the spectra for I_{DC} values up to 10 mA. The use of TRSKM as a direct probe of localized modes of microscale devices in SOT-FMR measurements goes beyond the spatially averaged capability of popular electrical measurement techniques and paves the way toward spatially resolved measurements of SOT.

5. Quasi-static magnetization investigation for DC SOT

5.1 The Planar Hall study

This chapter presents a further study into the dynamics excited by DC SOT employing a bi-polar square wave pulse. Furthermore, the Planar Hall effect (PHE) measurement connects the magnetoresistance response with the direct optical detection of the out-of-plane in the MOKE measurement. The qualitative comparison between the PHE field scan and the polar MOKE measurements will be discussed. The polar MOKE signal in the graphs below is normalised to the value corresponding to full out of plane magnetization, so that the magnitude of the SOT at the specified current density can be determined.

The magnetoresistive response of the device is measured during a field scan to determine the coercivity field value of the magnetic ellipse. The magnetic field scan is separated into sections, the first starts the field from zero and reaches the maximum field. Later, the field values are reduced, then increased to the opposite polarity and then the field is swept again towards the maximum field value. In summary, we have two fully swept fields from one maximum value to the other maximum value of opposite polarity. Last section of the scan the field is reduced back to zero.

For our experiments, we have selected the device's size of $1000 \times 400 \text{ nm}^2$. The electrical probes are landed along the edge of the gold leads that extend to the Platinum Hall cross. The current electrical probes are connected with a BNC-to-SMA cable to a (Keithley) current generator. The current's direction is parallel to the HA axis of the ellipsoid thus the DC Oe-field is parallel with the spin polarization. The Hall probes are landed in the other gold leads, that connect the long axis of the ellipse. The nano-voltmeter is also connected parallel to the 2 kOhms resistance and the Hall probes. The setup is discussed in Chapter 3 and presented in Figure 3.2.

In the optical measurements, we use only the current probe, connected with a function generator, that applies a square wave current pulse modulated at 3.14 kHz. The optical detection is the 400 nm laser pulse that comes perpendicular to the surface of the sample. The reflected elliptically polarized beam is directed to a polarizing bridge detector. The signal is then analysed by a Glan-Thompson beam splitter and the two photodiode detect the Kerr signal from the voltage difference. We can calibrate the detector by rotating it by 1 deg. and record the voltage difference. Before we begin a measurement, the detector is balanced (zero voltage difference) at zero field. The measured voltage difference from the field scans can be converted to Kerr rotation.

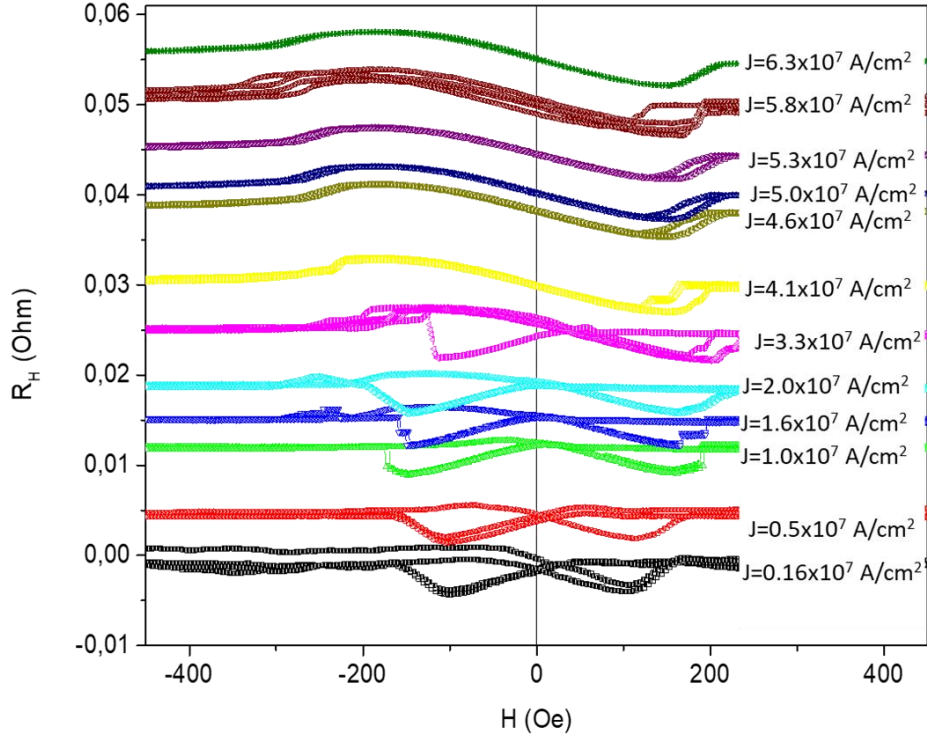


Figure 5.1: The planar hall effect (PHE) measurements as the magnetic field is swept at different current densities. The current density over the 4×10^7 A/cm² has shown a new behaviour where the magnetization changes from a butterfly shape to an S-shape loop. This characteristic indicates a preferred change around the EA during the field scan.

In the transport measurements the shape of curves from the field sweeps are related to the rotation magnetization of the plane. The S-shaped curves that are shown after current densities 4.1×10^7 A/cm² indicate a preference of specific rotation over the EA in the normal place. The S-shaped curves look like half a butterfly curve. The size of the ellipse in the devices presented in fig. 5.1 is 1000×400 nm². On the sample, we performed Planar Hall effect (PHE) measurements to determine the H_c for this device. In Fig.5.1 the measured THE voltage is plotted against an applied field along the HA (z)-axis. From an analytical solution we presented the eq. 3.18 for the THE voltage

$$V_x \propto H_z - H_c \sqrt{1 - \frac{(H-H_c)}{2}},$$

we can estimate the H_c value for this device being $H_c = 132$ Oe for the measured PHE seen in fig. 5.1.

The wafer has numerous devices with different sizes and designs. On the specific design, PHE we performed in all different sizes. The sizes measured, were 50×150 , 60×180 , 75×200 , 200×500 , 400×1000 , 800×2000 and 2000×5000 nm², respectively. The transport measurement performed on each device size can be used to extract a coercivity field value. The figure 5.2 shows the change of coercivity with increasing the device's length. The graph presents that smaller devices have higher coercivity field value. The relation between the two quantities is shown to best relation by a hyperbolic fit.

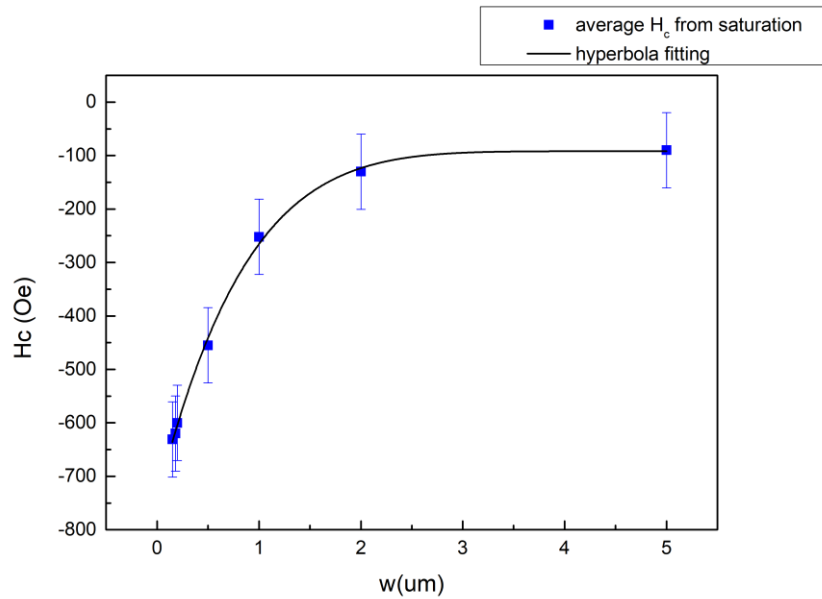


Figure 5.2: The diagram represents data extracted from the PHE measurements for the coercive field value over size. The H_c is increasing significantly with respect to size of ferromagnetic ellipsoid. The fitting use indicate a hyperbola change with respect to size.

The results from transport measurement show a variation with respect to coercive field value (H_c). The H_c is increasing with reducing size. For our numerical calculations, is interest the two sizes for $1000 \times 400 \text{ nm}^2$. One in the PHE field scan for the $2000 \times 800 \text{ nm}^2$ the expect was -130 Oe while in SOT-FMR the selected value of $H_c = -135 \text{ Oe}$. This important parameter is expected to be similar in Quasi-Static MOKE measurements.

5.2 Quasi-static MOKE measurement

In this configuration, the electrical current is driving the SOT response of the device as the current passes through the Platinum. The in-plane magnetized ellipsoid layer on top of the Platinum Hall cross will sense the spin accumulation in the HM. Our hypothesis on the spin dynamics is that is dominated by the DC-Oersted field and the SOT torque acting on the magnetization. The pulse laser beam is probing from the perpendicular direction to the sample plane, it selectively detects the polar component of the magnetization as the MOKE signal.

The optical Kerr signal will help in the investigation as it can be locally probed and detect the local and non-local phenomena that arise from electrical excitations. Additionally, with the sample upon the scanning stage, we can extract the behaviour of such dynamic systems with a resolution limited by the size of the optical probe. The spatial resolution of our scanning is only limited by the laser pulse width. The TRSKM experimental set up is designed to exploit the MOKE response and can be used as a

powerful tool to extend our knowledge in the magnetic process on sub-nano and sub-micro scales.

Once the beam enters the microscope setup it passes through a polariser to ensure linear polarisation. The pulse is then directed and focused through a microscope objective onto the sample. An objective with a large numerical aperture is preferred as this produces a high angle of incidence. The diffraction limited beam of 400 nm width limited our optical measurements to devices of 1000x400 nm² and larger ellipses. The focused incident beam is then reflected carrying a small phase shift that change the polarization from linear to elliptical. The additional phase of the polarization is proportional to the changes of magnetization as the magnetic field is swept. The reflected beam passes again the objective lens, and it is redirected through a beam splitter into the bridge polarized detector, which consists of a polarising beam splitter and photo diodes. Light incident on the detector is split by the beam splitter into orthogonal polarisation components, and each resulting beam is aligned onto a diode. By using quadrant photo diodes, it is possible to infer the in-plane magnetisation, the mechanism for this will be described below.

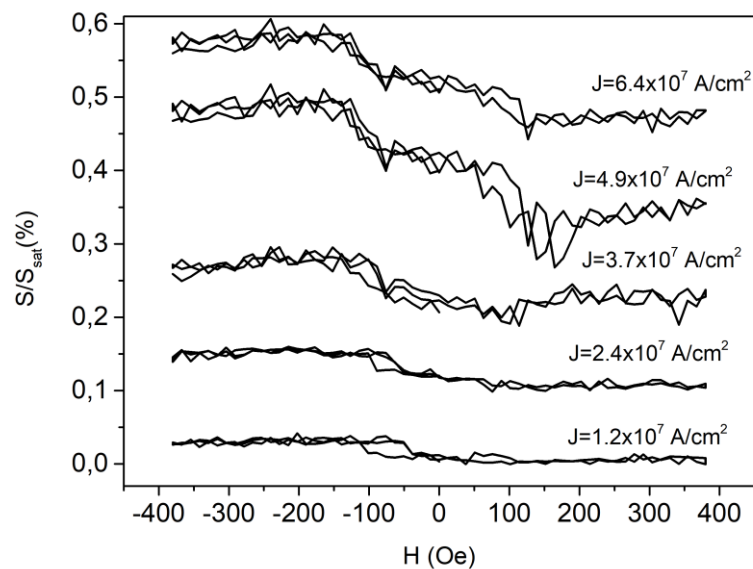


Figure 5.3: The field scans from the MOKE measurement that present the out-of-plane component of the magnetization with respect to applied magnetic field and increasing current density. The fields scan show that the amplitude of the polar Kerr signal increases with current density, but in a way that is inconsistent with the presence of only DC Oe-field contributions, suggesting that SOTs influence the detected signals. The probe spot set at the centre of the ellipse to detect the centre mode.

In the fig. 5.3 the field sweeps follow the sections we discussed earlier. The current densities contribute to the generation of the induced DC Oe-field and SOT. As discussed previously the amplitude response should be linear increased when the DC Oe-field is the dominant. However, it observed that increasing the current between the curve (fig.5.3) of $J=2.78 \times 10^7$ A/cm² and 4.15×10^7 A/cm², where the polar MOKE response of magnetization maybe affected by another mechanism. We take into

consideration the results in Chapter 4, assuming that the SOT effect is influencing the equilibrium magnetization as the higher current densities.

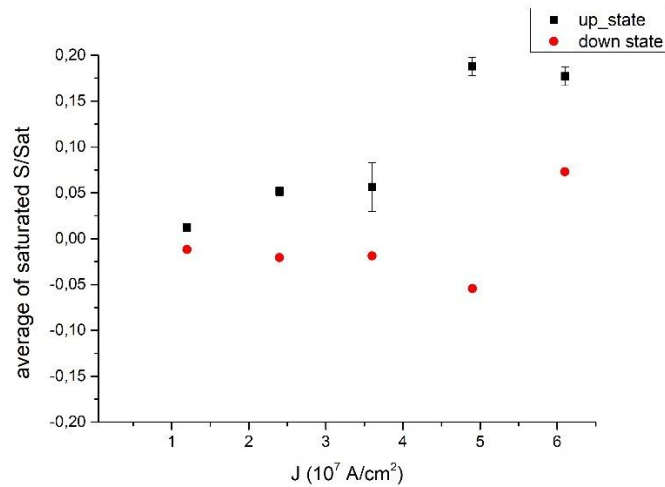


Figure 5.4: The average saturated magnetization values for either side of the applied field polarity for increasing current. The Polar MOKE response was measured from our QS MOKE measurements. The average values of the out-of-plane component show an average state of magnetization where for the given current density the magnetic component reached at saturation. The graph does show a non-linear response after current density over $5 \cdot 10^7$ A/cm².

The normalized values are a percentage of the out-of-plane component against the maximum, which measured in static Polar measurements. In Figure 5.4, the normalized values are shown with respect to the current density and each polarity. The normalized values are calculated from the Quasi-static MOKE field scan. The Fig.5.4 shows that the normalized saturated states with respect to the current densities are non-linear. Moreover, in current densities above $4.5 \cdot 10^7$ A/cm², the MOKE response is increased gradually. This indicates that damping-like SOT torque is dominant over DC Oe-field.

The MOKE response measured in Volts, it is converted to a Kerr rotation by using the calibration parameter (mdeg./V) extracted before each field scan. The normalized Kerr response is a Kerr rotation divided by the maximum out-of-plane rotation, which calculated at 82 mdeg. Thus, for each branch is 41 mdeg. Then the total response is a fraction of the maximum polar MOKE response (Figure 5.5). The normalized coefficient was taken from polar MOKE measurements on the unpatterned films. The saturation field of the out-of-plane component magnetization was shown by the field scan at 800 mT (fig. 5.5). A polar magnet was used for applying a perpendicular field up to 1 T. In our field scan measurements, the polar Kerr rotation is normalized with half the full swing.

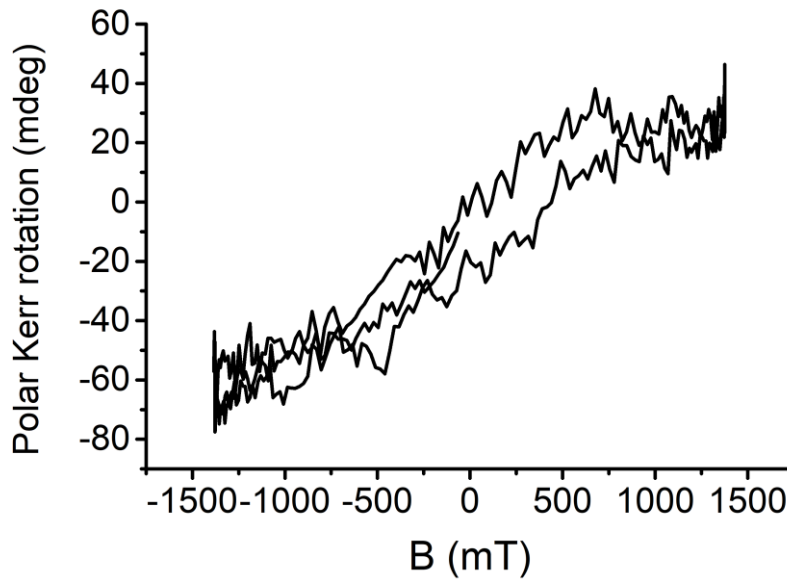


Figure 5.5: Polar MOKE measurements for the coupon samples. The Polar (perpendicular) magnet was sweeping the field from the from 0 to 1500 mT in the perpendicular direction to the magnetization plane. The Polar MOKE response measure to 82 mdeg. from the out of plane component.

The magnitude of ST can be calculated, while it will be depending on the current density thus, we find from ST value using the static from the analytical expression (3.1). Our understanding is the anti-damping torque of the SOT is dominant and the amplitude is between 0.8 to 4.2 Oe/A/cm². This assumption is encouraged by our macrospin model where the ST value was estimated to be significantly higher than FT. Therefore, the parameter FT is considered equal to zero, when we solved the analytical calculation to find an expression for the static out-of- plane magnetization component. However, we had preliminary results where the hysteresis loops with the quasi-static measurements did not show angular dependence. Our approach is similar to the approach that Z.Li et.al. had to investigate qualitatively and quantitatively the SOT torque in synthetic ferrimagnet. [69] The experiments of current-induced switching will be necessary to determine the magnitude of SOT torque.

5.3 Exploring the spatial resolution of spin dynamics.

The time-resolved scanning Kerr Microscope can measure the spatial resolution of the spatial MOKE response in the device's plane. In this configuration of the MOKE measurement, we could observe the spatial resolution of the device at a given magnetic field and current density. An interesting result from our measurement at the current density of 3.7 A/cm². The image scan we observed in the static applied field about $H_x = -126$ Oe at a current density of 4.9×10^7 A/cm².

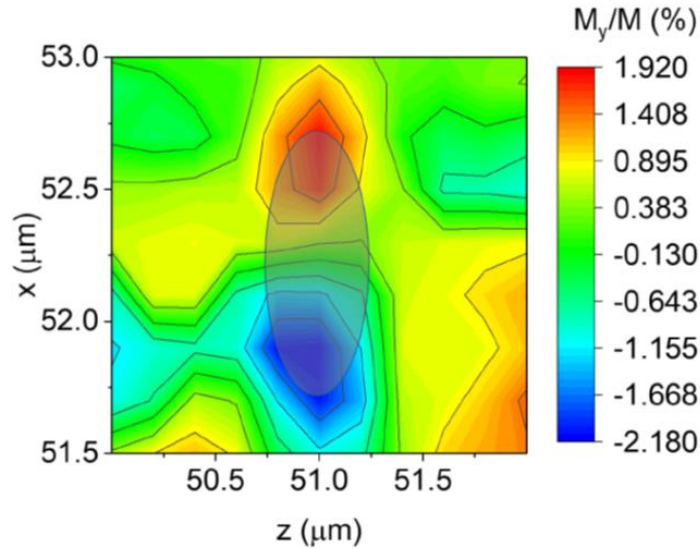


Figure 5.6: The spatial image of the device under current density and applied field. The observed asymmetry on the ellipsoid's (transparent ellipse) edge presents a dual response from a single ellipse element. This observation indicates that the equilibrium state breaks the single element response.

The imaging scan on figure 5.6 shows the asymmetry of the response we observed in the MOKE response as we probe from the centre of the ellipse. Performed two additional (Fig.5.7) field scan probes 200 nm above and below the centre of the ellipse will verify that the asymmetry and that probing from the centre of the ellipse is a superposition of two domains formed, that are linked to the current dependent metastable state of the equilibrium. on the next step we performed the field scan on the spots of the ellipse and measured the out-of-plane normalized Kerr signal. The graphs show that an internal spin dynamic presents a different response either way off the centre of the ellipse.

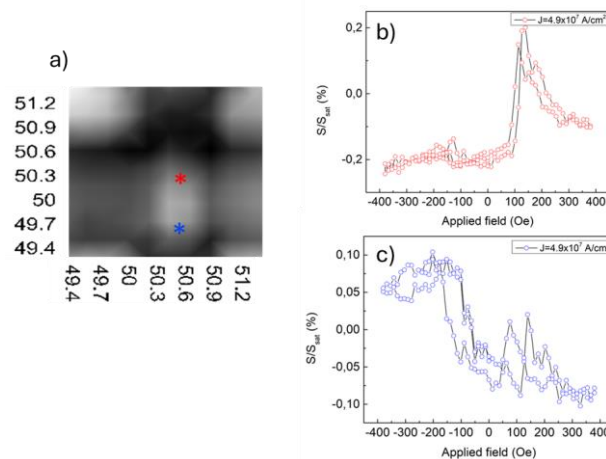


Figure 5.7: The image scan of the device before performing field at specific spot away from the centre of the ellipse. The asterisks indicated the position where we extracted the optical Kerr signal. The field scans for the lower and higher position from the centre of the ellipse. It is shown that the central mode is a superposition of the two dynamics that presented earlier in the static image.

The figure 5.7 present an image scan (with zero external field) of the device before performing field at specific spot away from the centre of the ellipse. We perform those image scan to make it verify we that the optical probe has not drift away from the device. The asterisks indicated the position where we extracted the optical Kerr signal. The field scans for the lower and higher position from the centre of the ellipse shown that the central mode is a superposition of the two internal dynamics.

Conclusions

In this thesis is presented the results of optically detected SOT-induced Ferromagnetic resonance and contribute results to the quantitative study for DC SOT on micro-sized in-plane magnetized ellipsoids. This study was conducted on SOT devices by utilizing the capabilities of a time-resolved scanning Kerr microscope (TRSKM). This stroboscopic approach allows us to investigate direct changes of the magnetization and visualise the local spin dynamics. This gives an advantage over traditional electrical methods where the measurement of magnetization dynamics was in-direct through magnetoresistance measurements.

The introduction chapter and the background chapter of this thesis gave the reader a brief introduction to the fundamental rules and basic information on the field of spintronics. The next chapter is described the experimental techniques used for our investigation. Chapter 4, the TRSKM has been used to perform optically detected, phase-resolved SOT-FMR measurements. the optical detection achieved from the geometric centre of the micro-sized ellipsoid probing the centre localized mode, where simultaneously reducing any non-uniform edge effects. Furthermore, the macro-spin model calculations reveal that a combination of both Oe-field and SOT is required to reproduce the marked asymmetry of the FMR spectra with respect to the polarity of the applied field. Additionally, we determined the values of the damping parameter and ST parameter.

In chapter 5, the TRSKM can be used to optically detect the local MOKE response induced by DC SOT in a semi-equilibrium state. The optical detection technique is also used to image the spatial resolution of macro magnetic devices. However, we were limited by the laser beam width to measure even smaller devices where it was expected the magnetic response would be uniform. In these presented results, the driving excitation is a DC step-function current that generates DC Oe-field and DC SOT to act on the magnetization of the macros-sized CoFeB ellipse element. We performed Planar Hall measurements that showed the change in the magnetic response as the current densities increased. The Quasi-Static MOKE measurement confirms this behaviour and probing from the centre of the ellipse minimizes nonuniform edge contributions in the Kerr signal. Based on the MOKE responses on the device we estimate that our SOT is $0.8 - 4.2 \text{ Oe/A/cm}^2$, and within the previous value, it has been estimated from our ferromagnetic resonance measurements. [31] Compared with the literature [31,36,45] value is within the range reported. This study is a step to a spatially resolved measurement of SOT that has been localized probed in microscale devices and proves capabilities over the spatial average response of the

electrical measurement techniques. Finally, we demonstrated the advantage of the TRSKM as a direct probe of localized modes on microscale devices go beyond the spatially averaged capability of popular electrical measurement techniques and paves the way toward spatially resolved measurements of SOT.

On Future work, we would like to investigate the optical detection of switching the device with high voltage (40 V) short pulse (~ 0.5 ps). This study will demonstrate the ability of SOT torque to fully switch the magnetization and contribute with results on features like low (write) power and higher speeds. Furthermore, micromagnetic simulations can give quantitative estimation for SOT torques on these devices and understanding of the internal mechanics.

Reference

- [1] S. A. Wolf, D. D. Awschalom, R. A. Buhrman, J. M. Daughton, S. von Molnár, M. L. Roukes, A. Y. Chtchelkanova, and D. M. Treger, *Spintronics: A Spin-Based Electronics Vision for the Future*, Science **294**, 1488 (2001).
- [2] Sabpreet Bhatti, Shunsuke Fukami, S.N. Piramanayagam, and Rachid Sbiaa, Atsufumi Hirohata, Hideo Ohno, *Spintronics Based Random Access Memory: A Review*, Materials Today **20**, (2017).
- [3] Y. Shiroishi, K. Fukuda, I. Tagawa, H. Iwasaki, S. Takenoiri, H. Tanaka, H. Mutoh, and N. Yoshikawa, *Future Options for HDD Storage*, IEEE Transactions on Magnetism **45**, 3816 (2009).
- [4] A. Brataas, A. D. Kent, and H. Ohno, *Current-Induced Torques in Magnetic Materials*, Nature Materials **11**, 372 (2012).
- [5] K. Garello, I. M. Miron, C. O. Avci, F. Freimuth, Y. Mokrousov, S. Blügel, S. Auffret, O. Boulle, G. Gaudin, and P. Gambardella, *Symmetry and Magnitude of Spin–Orbit Torques in Ferromagnetic Heterostructures*, Nature Nanotechnology **8**, 587 (2013).
- [6] M. N. Baibich, J. M. Broto, A. Fert, F. N. Van Dau, F. Petroff, P. Etienne, G. Creuzet, A. Friederich, and J. Chazelas, *Giant Magnetoresistance of (001)Fe/(001)Cr Magnetic Superlattices*, Phys. Rev. Lett. **61**, 2472 (1988).
- [7] J. Åkerman, *Toward a Universal Memory*, Science **308**, 508 (2005).
- [8] Tom Coughlin, *20b Emerging Memory Marketby 2029*, <https://www.forbes.com/sites/tomcoughlin/2019/07/09/20b-emerging-memory-market-by-2029/>.
- [9] Tom Coughlin, *Latest Emerging Memory Developments At 2021 IEDM And MRAM Forum Including In Memory Computing*, <https://www.forbes.com/sites/tomcoughlin/2021/12/27/latest-emerging-memory-developments-at-2021-iedm-and-mram-forum-including-in-memory-computing/>.
- [10] Joel Hruska, *Nvidia Unveils Ampere A100 80GB GPU With 2TB/s of Memory Bandwidth*, <https://www.extremetech.com/computing/317397-nvidia-unveils-ampere-a100-80gb-gpu-with-2tb-s-of-memory-bandwidth>.
- [11] NVIDIA, *Accelerating the Most Important Work of Our Time*, <https://www.nvidia.com/en-us/data-center/a100/>.
- [12] NVIDIA, *NVIDIA A100 Tensor Core GPU Architecture-Whitepapers*, (2020).
- [13] H. Chen, X. Fan, W. Wang, H. Zhou, Y. S. Gui, C.-M. Hu, and D. Xue, *Electric Detection of the Thickness Dependent Damping in Co90Zr10 Thin Films*, Applied Physics Letters **102**, 202410 (2013).

- [14] U. H. Pi, K. Won Kim, J. Y. Bae, S. C. Lee, Y. J. Cho, K. S. Kim, and S. Seo, *Tilting of the Spin Orientation Induced by Rashba Effect in Ferromagnetic Metal Layer*, Applied Physics Letters **97**, 162507 (2010).
- [15] P. Yu and M. Cardona, *Fundamentals of Semiconductors* (Springer-Verlag Berlin Heidelberg, 2003).
- [16] Allan H. Morrish, *The Physical Principles of Magnetism* (R. E. Krieger Publishing Company, 1980, n.d.).
- [17] X. Fan, T. G. Myers, B. A. D. Sukra, and G. Gabrielse, *Measurement of the Electron Magnetic Moment*, Phys. Rev. Lett. **130**, 071801 (2023).
- [18] Stephen Blundell, *Magnetism in Condensed Matter* (Oxford University Press, 2001).
- [19] Alex Hubert and Rudolf Schaefer, *Magnetic Domains: The Analysis of Magnetic Microstructures* (Springer Berlin, Heidelberg, 2008).
- [20] Joachim Stöhr and Hans Christoph Siegmann, *Magnetism: From Fundamentals to Nanoscale Dynamics N Authors*, (Springer-Verlag Berlin Heidelberg 2006, 2006).
- [21] J. Crangle, *The Magnetic Properties of Solids* (Edward Arnold, 1977).
- [22] J.A.C. Bland and B. Heinrich, *Ultrathin Magnetic Structures I An Introduction to the Electronic, Magnetic and Structural Properties* (n.d.).
- [23] G. Dresselhaus, *Spin-Orbit Coupling Effects in Zinc Blende Structures*, Phys. Rev. **100**, 580 (1955).
- [24] Griffiths J. H. E, *Anomalous High-Frequency Resistance of Ferromagnetic Metals*, (n.d.).
- [25] Charles Kittel., *On the Theory of Ferromagnetic Esonance Absorption*, Physical Review **73**, 155 (1948).
- [26] L. Landau and E. Lifshits, *On the Theory of the Dispersion of Magnetic Permeability in Ferromagnetic Bodies*, Phys. Zeitsch. Der Sow **169**, 14 (1935).
- [27] Gilbert, T. L., *A Phenomenological Theory of Damping in Ferromagnetic Materials.*, IEEE Transactions on Magnetics, **40**, 3443 (2004).
- [28] J. Slonczewski, *Current-Driven Excitation of Magnetic Multilayers*, J. Magn. Magn. Mater. **159**, L1 (1996).
- [29] S. Zhang, P. M. Levy, and A. Fert, *Mechanisms of Spin-Polarized Current-Driven Magnetization Switching*, Phys. Rev. Lett., **88**, 236601 (2002).
- [30] A. A. Tulapurkar, Y. Suzuki, A. Fukushima, H. Kubota, H. Maehara, K. Tsunekawa, D. D. Djayaprawira, N. Watanabe, and S. Yuasa, *Spin-Torque Diode Effect in Magnetic Tunnel Junctions*, Nature **438**, 339 (2005).

- [31] P. S. Keatley, K. Chatzimpaloglou, T. Manago, P. Androvitsaneas, T. H. J. Loughran, R. J. Hicken, G. Mihajlović, L. Wan, Y. Choi, and J. A. Katine, *Optically Detected Spin–Orbit Torque Ferromagnetic Resonance in an in-Plane Magnetized Ellipse*, Applied Physics Letters **118**, 122405 (2021).
- [32] J.. E. Hirsch, *Spin Hall Effect*, Phys. Rev. Lett. **83**, 1834 (1999).
- [33] R. C. Myers, Y.K..Kato, A.C. Gossard, and D. D. Awschalom, *Observation of the Spin Hall Effect in Semiconductors.*, Science **306**, 1910 (2004).
- [34] J.Wunderlich, B. Kaestner, J. Sinova, and T. Jungwirth, *Experimental Observation of the Spin-Hall Effect in a Two-Dimensional Spin-Orbit Coupled Semiconductor System*, Physical Review Letters **94**, 047204 (2005).
- [35] A. Hoffmann, *Spin Hall Effects in Metals*, IEEE Transactions on Magnetics **49**, 5172 (2013).
- [36] G. Mihajlović, O. Mosendz, L. Wan, N. Smith, Y. Choi, Y. Wang, and J. A. Katine, *Pt Thickness Dependence of Spin Hall Effect Switching of In-Plane Magnetized CoFeB Free Layers Studied by Differential Planar Hall Effect*, Applied Physics Letters **109**, 192404 (2016).
- [37] L. Liu, T. Moriyama, D. C. Ralph, and R. A. Buhrman, *Spin-Torque Ferromagnetic Resonance Induced by the Spin Hall Effect*, Phys. Rev. Lett. **106**, 036601 (2011).
- [38] J. Kim, J. Sinha, M. Hayashi, M. Yamanouchi, S. Fukami, T. Suzuki, S. Mitani, and H. Ohno, *Layer Thickness Dependence of the Current-Induced Effective Field Vector in Ta|CoFeB|MgO*, Nature Materials **12**, 240 (2013).
- [39] I. Mihai Miron, G. Gaudin, S. Auffret, B. Rodmacq, A. Schuhl, S. Pizzini, J. Vogel, and P. Gambardella, *Current-Driven Spin Torque Induced by the Rashba Effect in a Ferromagnetic Metal Layer*, Nature Materials **9**, 230 (2010).
- [40] A. Manchon, H. C. Koo, J. Nitta, S. M. Frolov, and R. A. Duine, *New Perspectives for Rashba Spin–Orbit Coupling*, Nature Materials **14**, 871 (2015).
- [41] P. Grünberg, R. Schreiber, Y. Pang, M. B. Brodsky, and H. Sowers, *Layered Magnetic Structures: Evidence for Antiferromagnetic Coupling of Fe Layers across Cr Interlayers*, Phys. Rev. Lett. **57**, 2442 (1986).
- [42] I. A. Campbell and A. Fert, “*Transport Properties of Ferromagnets,*” Ferromagnetic Materials,(North-Holland, Amsterdam) **3**, 747 (1987).
- [43] M. Julliere, *Tunneling between Ferromagnetic Films*, Physics Letters A **54**, 225 (1975).
- [44] D. C. Ralph and M. D. Stiles, *Spin Transfer Torques*, Journal of Magnetism and Magnetic Materials **320**, 1190 (2008).
- [45] M. Cubukcu, O. Boulle, M. Drouard, K. Garello, C. Onur Avci, I. Mihai Miron, J. Langer, B. Ocker, P. Gambardella, and G. Gaudin, *Spin-Orbit Torque Magnetization*

Switching of a Three-Terminal Perpendicular Magnetic Tunnel Junction, Applied Physics Letters **104**, 042406 (2014).

[46] R. P. Cowburn, *The Attractions of Magnetism for Nanoscale Data Storage*, Philosophical Transactions of The Royal Society A, **358:12**, (2003).

[47] T. Endoh, H. Honjo, K. Nishioka, and S. Ikeda, *Recent Progresses in STT-MRAM and SOT-MRAM for Next Generation MRAM*, in *2020 IEEE Symposium on VLSI Technology* (2020), pp. 1–2.

[48] Anton Shilov, *TSMC Tandem Builds Exotic New MRAM-Based Memory with Radically Lower Latency and Power Consumption*, <https://www.tomshardware.com/pc-components/dram/tsmc-tandem-builds-exotic-new-memory-with-radically-lower-latency-and-power-consumption-mram-based-memory-can-also-conduct-its-own-compute-operations>.

[49] Sankey, J., P. M., Garcia, C., Braganca, A. G., Krivorotov, and I. N., Buhrman, R. A., & Ralph, D. C., *Spin-Transfer-Driven Ferromagnetic Resonance of Individual Nanomagnets*, Physical Review Letters **96**, 227601 (2006).

[50] H. Kubota et al., *Quantitative Measurement of Voltage Dependence of Spin-Transfer Torque in MgO-Based Magnetic Tunnel Junctions*, Nature Physics **4**, 37 (2008).

[51] T. Spicer et al., *Spatial Mapping of Torques within a Spin Hall Nano-Oscillator*, Physical Review B **98**, (2018).

[52] T. M. Spicer et al., *Time Resolved Imaging of the Non-Linear Bullet Mode within an Injection-Locked Nano-Contact Spin Hall Nano-Oscillator*, Applied Physics Letters **113**, 192405 (2018).

[53] Rae, M.E. and Kryder, M.H., *Magneto-Optic Investigation of Thin-Film Recording Heads.*, Journal of Applied Physics **55**, 2245 (1984).

[54] P. Gangmei, P. S. Keatley, W. Yu, R. J. Hicken, M. A. Gubbins, P. J. Czoschke, and R. Lopusnik, *Time- and Vector-Resolved Kerr Microscopy of Hard Disk Writers*, Applied Physics Letters **99**, 232503 (2011).

[55] P. S. Keatley, V. V. Kruglyak, A. Neudert, E. A. Galaktionov, R. J. Hicken, J. R. Childress, and J. A. Katine, *Time-Resolved Investigation of Magnetization Dynamics of Arrays of Nonellipsoidal Nanomagnets with Nonuniform Ground States*, Phys. Rev. B **78**, 214412 (2008).

[56] Y. Tserkovnyak, A. Brataas, and G. E. W. Bauer, *Enhanced Gilbert Damping in Thin Ferromagnetic Films*, Phys. Rev. Lett. **88**(11), 117601 (2002).

[57] M. K. Marcham et al., *Phase-Resolved x-Ray Ferromagnetic Resonance Measurements of Spin Pumping in Spin Valve Structures*, Phys. Rev. B **87**, 180403 (2013).

[58] J. Li et al., *Direct Detection of Pure Ac Spin Current by X-Ray Pump-Probe Measurements*, Phys. Rev. Lett. **117**, 076602 (2016).

- [59] Y. Otani and T. Kimura, *Manipulation of Spin Currents in Metallic Systems*, Philosophical Transactions of the Royal Society A: Mathematical, Physical and Engineering Sciences **369**, 3136 (2011).
- [60] T. Kimura, Y. Otani, and J. Hamrle, *Switching Magnetization of a Nanoscale Ferromagnetic Particle Using Nonlocal Spin Injection*, Phys. Rev. Lett. **96**, 037201 (2006).
- [61] T. Yang, T. Kimura, and Y. Otani, *Giant Spin-Accumulation Signal and Pure Spin-Current-Induced Reversible Magnetization Switching*, Nature Physics **4**, 851 (2008).
- [62] L. Liu, O. J. Lee, T. J. Gudmundsen, D. C. Ralph, and R. A. Buhrman, *Current-Induced Switching of Perpendicularly Magnetized Magnetic Layers Using Spin Torque from the Spin Hall Effect*, Phys. Rev. Lett. **109**, 096602 (2012).
- [63] C. Stamm, C. Murer, M. Berritta, J. Feng, M. Gabureac, P. M. Oppeneer, and P. Gambardella, *Magneto-Optical Detection of the Spin Hall Effect in Pt and W Thin Films*, Phys. Rev. Lett. **119**, 087203 (2017).
- [64] O. Fruchart and A. Thiaville, *Magnetism in Reduced Dimensions*, Comptes Rendus Physique **6**, 921 (2005).
- [65] T. D. Skinner, M. Wang, A. T. Hindmarch, A. W. Rushforth, A. C. Irvine, D. Heiss, H. Kurebayashi, and A. J. Ferguson, *Spin-Orbit Torque Opposing the Oersted Torque in Ultrathin Co/Pt Bilayers*, Applied Physics Letters **104**, 062401 (2014).
- [66] C. Sankey, Y.-T. Cui, J. Z. Sun, and J. C. Slonczewski, R. a. Buhrman, and D. C. Ralph, *Measurement of the Spin-Transfer-Torque Vector in Magnetic Tunnel Junctions*, Nature Physics **4**, 67–71 (2008) **4**, 67 (2008).
- [67] R. Dumas, S. R. Sani, S. M. Mohseni, E. Iacocca, Y. Pogoryelov, P. K. Muduli, S. Chung, P. Dürrenfeld, and J. Åkerman, *Recent Advances in Nanocontact Spin-Torque Oscillators*, IEEE Transactions on Magnetics **50**, 1 (2014).
- [68] S. S. Kalarickal, P. Krivosik, M. Wu, C. E. Patton, M. L. Schneider, P. Kabos, T. J. Silva, and J. P. Nibarger, *Ferromagnetic Resonance Linewidth in Metallic Thin Films: Comparison of Measurement Methods*, Journal of Applied Physics **99**, 093909 (2006).
- [69] Z. Li et al., *Highly Efficient Spin-Orbit Torque in a Perpendicular Synthetic Ferrimagnet*, Phys. Rev. B **105**, 184419 (2022).